3D-Printed Multi-Channel Scaffolds for Investigating the Foreign Body Response

Yuto Koga

A thesis
submitted in partial fulfillment of the
requirements for the degree of

Master of Science in Bioengineering

University of Washington

2025

Committee:

Buddy D. Ratner

James D. Bryers

Albert Folch

Program Authorized to Offer Degree:

Bioengineering

University of Washington

Abstract

3D-Printed Multi-Channel Scaffolds for Investigating the Foreign Body Response

Yuto Koga

Chair of the Supervisory Committee:

Buddy D. Ratner

Department of Bioengineering

Department of Chemical Engineering

The success of implantable biomaterials is often limited by the foreign body response (FBR), a chronic immune reaction that results in a thick, fibrous capsule that sometimes leads to complete implant failure. Recent research has demonstrated the importance of porosity to mitigate the FBR; however there is much that is still unknown regarding the role that porosity, and the channel regions in between the pores have on the FBR. As such, porous scaffolds with 40 µm rectangular channels of different sizes were designed and fabricated using a stereolithography (SLA) 3D printing approach. By adjusting the printing modulation, velocity and focus values, we demonstrated the capability to produce various porous scaffold designs with high precision in a single print. Furthermore, additional *in vivo* studies showcased that these porous scaffolds with a 40 µm cubical cross-section, rectangular channels can reduce the fibrotic capsule thickness, albeit at lower levels of cellularization. This research showcased, however, the potential for utilizing 3D printers to create new porous scaffolds, and provided valuable information towards engineering biomaterials to better mitigate the foreign body response.

Table of Contents

LIST OF FIGURES

LIST OF TABLES

LIST OF SUPPLEMENTARY FIGURES

ACKNOWLEDGEMENTS

I'd like to first thank my advisor, Dr. Buddy Ratner, for accepting me into his lab and guiding me for these past two years. His constant support and vision for my project allowed me to learn so much and reach the milestones I aspired to reach since my first year of graduate school, and I would not be where I am without his thoughtful discussions and insights about the direction of my research. I'd also like to give a massive thank you to Guoyao Chen, who gave me great guidance on how to operate all equipment, all of the experimental techniques, as well as various tips and suggestions to help troubleshoot all of the various challenges I faced throughout the course of this research project. I'd also like to thank Sharon Creason for all the help she has provided to me, from initially helping with the onboarding, to helping with all of the animal surgery procedures, Louis Chen for assisting with conducting the tissue sectioning and staining experimental portions, and the entire Ratner research group for their constant support, assistance and feedback throughout these past two years. Finally, I'd like to thank my parents Maya Endoh and Tadanori Koga, as well as my siblings Maho Koga, Leio Koga and Kyto Koga for their endless love and support.

This work was supported by the Department of Bioengineering at the University of Washington.

CHAPTER 1: INTRODUCTION

1.1 ENGINEERED BIOMATERIALS AND THE FOREIGN BODY RESPONSE

Within the past decade, significant advancements have been made to better engineer biomaterials. For instance, numerous research groups have demonstrated improved integration of biomaterials into tissue by incorporating additional chemical modalities into their surfaces[1-3], or enhanced the regenerative capabilities of scaffolds by altering the surface topography[4-6]. These advancements illustrate the broader trend in biomaterials research to develop improved implantable systems that are more functional[5, 7, 8] and more importantly, better integrated with the human body[8-10], in hopes to ultimately develop the next-generation of implants that can promote a more favorable healing response at the implant site.

Despite these advancements, many of these materials still initiate the foreign body reaction (FBR), which is a complex, multi-phase immune response, traditionally divided into acute and chronic stages[8, 11-14]. In the acute stage, which begins immediately after the implantation sequence, blood proteins adsorb onto the implant surface, subsequently leading to the formation of a provisional matrix. This initiates the recruitment of neutrophils and polymorphonuclear leukocytes to the implant site[11, 14], where they interact with the matrix-bound factors and degranulate, thereby triggering the release of proteolytic enzymes and reactive oxygen species (ROS). This process is intended to degrade and ultimately remove the foreign object; however, the inability to break down many of these implanted materials leads to prolonged inflammatory stimuli, thereby driving the transition to the chronic inflammation stage of the FBR, marked by infiltration of the implant site with mononuclear cells, such as monocytes and lymphocytes.

During this chronic stage, circulating monocytes are recruited to the implant site and differentiate into macrophage cells, one of the central mediators of the FBR. Upon activation, these macrophages secrete other chemokines such as IL-8, MCP-1, and MIP-1β[14, 15], which drives other inflammatory cells towards the implant site. Eventually, the prolonged adherence and activation of macrophages at the implant site, coupled with their continued inability to phagocytose the foreign material, leads the macrophage cells to fuse into multinucleated foreign body giant cells (FBGCs), thereby activating fibroblast cells. Ultimately, these processes result in the formation of dense, avascular fibrous capsule, which continues to thicken over time until the implant is completely isolated from the surrounding tissue. Although the inflammatory process may recede, the resulting encapsulation of the implant typically results in implant functionality loss and/or complete implant failure[8, 11-14], which highlights the importance of preventing this reaction.

Despite this well-characterized understanding of the FBR[8, 11-15], it is estimated that roughly 10% of all implants fail due to the FBR, translating in upwards of 10 billion dollars annually in additional healthcare costs in the United States alone[16]. Fortunately, many approaches have been developed to better engineer materials to minimize the FBR. For example, Tan et al. coated their implantable material with various extracellular matrix molecules, such as fibronectin (FN) and IL-4, which generated a thinner fibrotic capsule compared to control polyethersulfone implants[17]. Others, such as Barr et al., produced patterned PDMS implants, which subsequently improved the polarization of macrophage cells towards the pro-healing phenotypes (M2)[18]. Additionally, there are numerous reviews detailing other approaches[8, 16, 19], such as utilizing low-fouling (anti-fouling) materials[16], or producing material that release anti-fibrotic agents[20], which highlights the versatility there is in minimizing the extent of the FBR.

To date, one of the most promising approaches to mitigate the FBR revolves around the development of porous biomaterials[21, 22]. These porous materials are composed of two parts: the pore (the void area) and an interconnecting / channel region (the spaces or channels that link the individual pores within the scaffold). There have been a variety of porous scaffolds created with a different shapes[23-27], sizes[27-29], porosity ratios[30, 31], and

materials[31-34], and the unique ability to fabricate these materials and scaffolds either through subtractive techniques (like spherical templating[24, 25, 35], salt leaching[36], or freeze casting[37, 38]) or additive techniques (like 3D printing[5, 39], electrospinning[40, 41] , and gas foaming[42]) provides unparalleled flexibility to tailor the properties and architectures of these porous scaffolds to meet specific applications. Most importantly, these porous scaffolds have proven in numerous applications[21, 23-25, 28, 34, 41, 43, 44] to exhibit favorable tissue responses. Although the exact mechanism for why these porous scaffolds promote favorable tissue response is widely discussed, many believe that the ability of cells to infiltrate into the material through the pores plays a significant role in this process.

More specifically, it's believed that the elongation and subsequent contraction of the macrophage cytoskeleton as they pass through the porous areas drives macrophage polarization towards the alternative (M2) state, which is in opposition to the classically activated M1 phenotype, which is traditionally expressed during the inflammatory and/or degradative periods of the FBR[13, 14, 22, 24, 35, 45-48]. This theory was observed separately by McWhorter et al., where they noted that increased cellular elongation via artificial stimulation led to a higher expression of CD206, arginase-1 and YM-1, all of which are markers for M2 polarization[46], which further demonstrated that while there may be other underlying factors behind this pore-mediated healing response [23, 25], based on this research, the elongation of the macrophage cells is a pivotal step in prompting a pro-regenerative immune environment.

Within our research group, extensive efforts have been dedicated to utilizing these porous materials for sub-cutaneous and percutaneous applications, specifically in hopes to develop improved arteriovenous (AV) grafts for hemodialysis applications[49-51]. Furthermore, recent research from our group and others at the University of Washington has shown that for subcutaneous[22, 24, 25, 35, 43, 51], percutaneous[50] and cardiac[44] applications, porous structures with 40 µm pore sizes across various material types exhibit higher levels of angiogenesis and cellularization, and more notably, minimizes the thickness of the fibrotic capsule. Most recently, this behavior was also observed in 3D printed porous structures containing 40 µm pores[26, 51], which now enables the production of these porous scaffolds without requiring the previously used bead sintering techniques[26, 51, 52], which was challenging and time-consuming. For instance, whereas producing a porous scaffold with the bead sintering technique may have taken two weeks to produce, with the stereolithography (SLA) printer we currently employ, we can produce structures with a higher degree of control in just a few hours.

However, despite the advances our lab group has made to create new structures using the 3D printer, there still remains many challenge in producing porous structures with smaller pore and/or interconnecting regions with high resolution[26, 51]. More specifically, previous attempts to create uniform structures with these smaller interconnecting region led to the creation of incomplete shapes in the printed structure and/or resulted in porous structures that had several fluctuations in pore size[26]. Additionally, as we look to continue to explore the role pore design (elements such as pore geometry, interconnecting regions, channel size, etc.) has towards mitigating the foreign body reaction, it is imperative for us to be able to fabricate more sophisticated structures with greater precision, which currently, we are unable to do.

Likewise, recent research has also focused on identifying new ways to reduce the overall use of animal experiments, in accordance with the University of Washington's 3R goals. Although it is difficult to model the full extent of the foreign body reaction in vitro, with the recent incorporation of the 3D printer to produce porous scaffolds, we questioned whether it was possible now to create a new type of porous scaffold that contained multiple different scaffold designs or architectures within a single device, in order to enable concurrent *in vivo* testing of different variables without requiring additional animals.

As such, here, we looked to create a new type of porous scaffold that contained porous channels of varying lengths (40 µm, 80 µm, & 120 µm) within a singular device, in order to assess whether these porous scaffolds could still produce similar levels of healing compared to the spherical porous structures previously created in subcutaneous applications. Although these structures no longer contain the smaller 16 µm

interconnecting regions previously used[22, 24, 25, 35, 43, 51], based on the success of others to utilize similar porous scaffolds with uniform channels in bone regeneration applications[53-55], as well as the overall excellent display of these scaffolds to regulate the distribution of chemicals and cells throughout their design[56], and lastly, the ability to potentially elongate macrophage cells in box-shaped scaffolds *in vitro*[47], we hypothesized that these new scaffolds, particularly in the scaffolds with the 40 µm channels, could preserve similar levels of healing compared to the historically used scaffolds. After implanting these scaffolds subcutaneously in mice over a four-week period, we then assessed the performance of these scaffolds to mitigate the foreign body reaction by quantifying the fibrotic capsule thickness and cellularization rates. Through this approach, we assessed the role of channel length on the foreign body response, and more importantly, determined the feasibility of using these multi-architecture porous scaffold as a new way to enable concurrent *in vivo* testing and reduce the overall need for animal experiments.

1.2 3D Printing Approach to Create Porous Biomaterials

There are numerous 3D printing (also known as additive manufacturing) methods utilized to create porous biomaterials. As shown in Figure 1, most of the 3D printing techniques fall within one of these six 3D printing techniques, and while it is theoretically possible to produce porous structures using any one of these printing techniques, many challenges exist in finding suitable printing modalities while considering material compatibility, desired resolution, accessibility and cost. For instance, Stereolithography (SLA) and Digital Light Processing (DLP) are two light-based techniques known for their high resolution and precision, making them particularly favorable for creating complex micro-porous structures with tunable geometries. Conversely, Fused Deposition Modeling (FDM) is one of the most accessible methods, and can be used to create porous scaffolds with well-defined macroporous networks, although its resolution is much lower compared to the aforementioned light-based systems. Alternatively, some researchers have opted to use Selective Laser Sintering (SLS) printing, as it utilizes a laser to fuse powdered materials without the need for support structures, thereby enabling users to create intricate and mechanically robust porous architectures[57, 58].

As aforementioned, we opted to use stereolithography to produce all of our 3D structures. SLA was first introduced by Charles Hull in the late 1980s[59], and despite the improvements made over the years, modern SLA printers rely on the same fundamental concepts as when first introduced. Briefly, SLA printers are built around three main components: the light source, the printing stage, and the printing vat. As showcased in Figure 2, for the KLOE Dilase 3D SLA printer used in this study, the light source (UV laser, 375 nm) only moves in the XY plane to selectively cure the liquid surface of a photopolymerizable resin. The printer also has a printing stage (the area where the structures were printed on) that moves up and down in the Z-direction, and the combination of the movements from the laser source and printing stage results in the fabrication of the 3D structures. Lastly, the Dilase 3D has a printing vat, which serves as a “housing unit” for the photopolymerizable resin, and the printing vat has a glass slide coated in polydimethylsiloxane (PDMS). This PDMS layer is critical to the success of the 3D prints, as the PDMS layer enables a thin layer of oxygen to form at the interface of the resin and the PDMS layer, which in turn, inhibits free radical polymerization. As such, there is a “dead zone” produced that ensures that any 3D printed structures would stick to and move with the printing vat and not the PDMS layer, which thereby ensures that the desired structures are printed as intended[26, 60, 61].

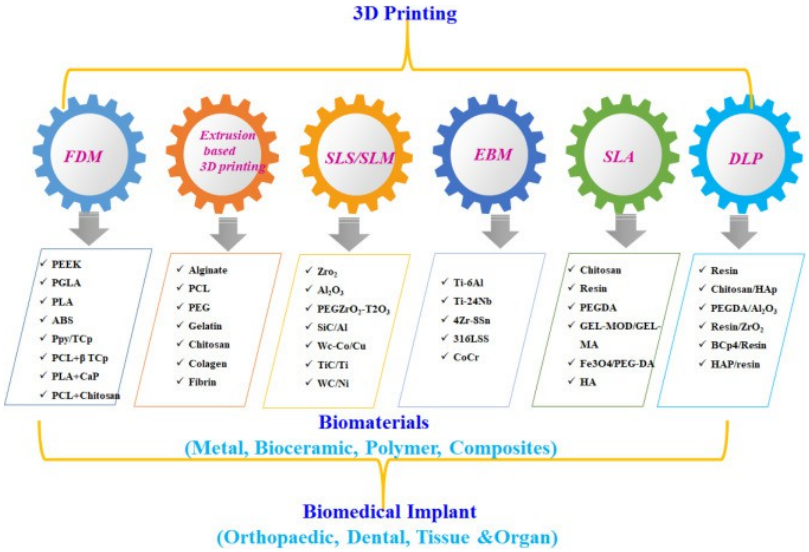

Figure 1: *Schematic illustration of the different 3D printing techniques to print biomaterials.* ***FDM****: Fused Deposition Modeling* ***SLS/SLM****: Selective Laser Sintering / Selecting Laser Melting* ***EBM****: Electron Beam Melting* ***SLA****: Stereolithography* ***DLP****: Digital Light Processing*
Credits: Ananth et al.[57]

While there are numerous SLA printing systems available commercially, the Dilase 3D was selected due to the several advantages it possesses over other SLA printers. Firstly, the resolution (measured by the smallest feature size that could be accurately cured) of the Dilase 3D printer is 5 µm, which is far superior to other SLA printers, which typically possesses a resolution in the range of around 20 µm to 100 µm[62]. Furthermore, the Dilase 3D supports a slicing pitch (measured by how "precisely" the printer could move in the Z-axis) of a few microns, which ensures that the resolution on the Z-axis is on par with the XY axis, and more importantly, that the resolution limits are far below the desired pore channel sizes, which thereby ensures that with optimized printing settings, it is theoretically possible to fabricate our porous structures with high precision. Lastly, the KLOE Dilase 3D printer also supports the use of the VITRA DS-2000 resin, which is a 3D printing resin commonly used in dental applications that previously has demonstrated excellent biocompatibility and left a smooth finish[26, 51], two factors

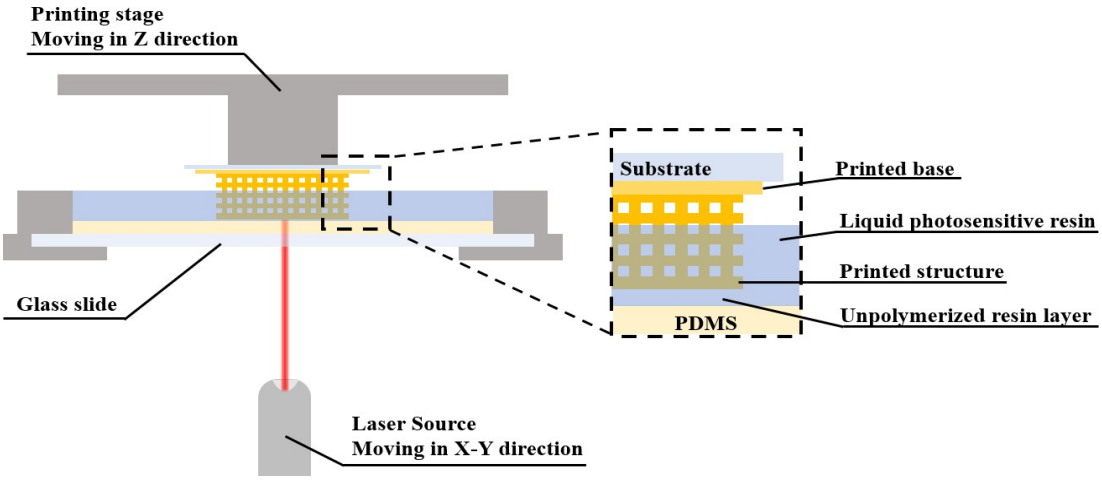

Figure 2: *Schematic illustration of how the SLA printer operates.* Credits: Guoyao Chen[26]

that are critical for mitigating the FBR. Thus, taken together, these advantages made the KLOE Dilase 3D printer the ideal choice for our research, where precision, biocompatibility, and reproducibility are paramount.

CHAPTER 2: EXPERIMENTAL APPROACH

2.1 MATERIALS

All materials used in this study are listed below, and were used as is, unless otherwise noted.

VITRA DS 2000 Resin (DWS, 10200075, 1L) was the sole 3D printing resin used in this study. Both 2-propanol (Fisher Chemical, A451-4, 4L) and ethanol (Decon Laboratories, Inc., 2701, 1 gal) were used to wash the printed scaffolds and remove residual resin from the printing vat. Sylgard 184 Elastomer Base (Electron Microscope Sciences, 24236-10A) and Sylgard 184 Elastomer Curing Agent (Electron Microscope Sciences, 230315-05) were used in conjunction to produce the PDMS film during the printing vat recoating process. Mason's Trichrome Stain kit was acquired from Tyr Scientific (Tyr Scientific, LOT # 80886) and was used to stain the sectioned samples for capsule thickness measurements. Hematoxylin and eosin (H&E) stain kit was purchased from Sigma-Aldrich (Sigma-Aldrich, LOT # SLBT4556, LOT# SLCC8965) and was used to stain the sectioned samples for cellularization.

2.2 DESIGN PROCESS FOR THE POROUS SCAFFOLDS (PS)

We designed all porous scaffolds in Blender™ 3D Software (The Blender Foundation, Blender Version 2.83). In total, three iterations of the porous scaffolds were created. Each porous scaffold contained four unique architectures (Table 1), where three of the architectures were porous and had a different channel length, and the last architecture was a non-porous unit. The dimensions for Porous Architecture A, B and C were chosen based on historical data; briefly, we knew that porous scaffolds with 40 µm pores had a more favorable FBR response, and thus, we decided to create three channels that were 40 µm in width and height, and then vary the length to be either 40 µm, 80 µm or 120 µm, in order to assess how the longer channel regions would impact the foreign body response. Lastly, we opted to also include the non-porous section as a positive control.

***Table 1**: Dimensions of the three-channel region architectures used in the porous scaffolds*

Porous Design	**Channel Dimensions**
Porous Architecture A	40 µm (L) x 40 µm (W) x 40 µm (H)
Porous Architecture B	80 µm (L) x 40 µm (W) x 40 µm (H)
Porous Architecture C	120 µm (L) x 40 µm (W) x 40 µm (H)
Porous Architecture D	N/A

2.2.1 DESIGN AND MODELING OF POROUS ARCHITECTURE A

In order to produce the Porous Architecture A design, which comprised of repeating rectangular channels that were 40 µm L x 40 µm W x 40 µm H channel (Figure 3A) in between two adjacent pores in all X, Y, Z directions, we first modeled an individual beam unit (40 µm L x 2000 µm W x 40 µm H) in Blender, and then duplicated the beam to form a planar array of beams with final lateral dimensions of 2000 µm × 2000 µm. To build out the full 3D structure, this planar array was then duplicated along the Z-direction using the same 40 µm spacing, in order to produce an array of beams that had the final dimensions of 2000 µm × 2000 µm × 4000 µm. The resulting beam

array was then duplicated and rotated twice more along orthogonal axes, and then the three arrays were overlayed on top of one another to form the final 3D grid architecture (Figure 3B and 3C).

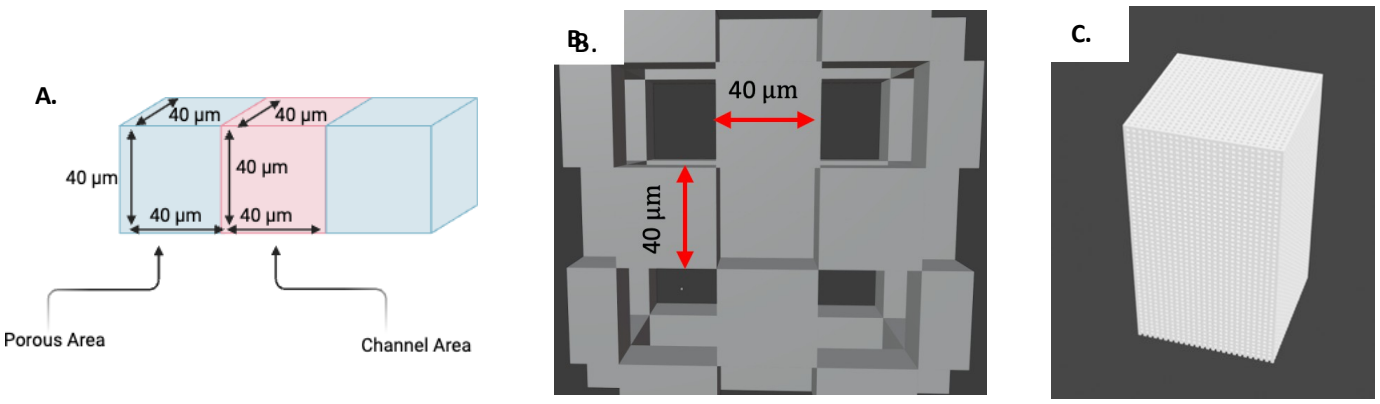

Figure 3A (left): *Schematic illustration of Porous Architecture A, and the dimensions of the porous areas and the channel area.* ***Figure 3B (middle):*** *Close up image of the truncated array of beams. As shown in the image, there is a 40 µm long channel surrounding each pore.* ***Figure 3C (right):*** *Zoomed out image of the final grid structure. The final dimensions of the grid structure is 2000 µm L x 2000 µm W x 4000 µm H.*

2.2.2 Design and Modeling of Porous Architecture B

The Porous Architecture B design was created in a similar fashion as described above. Briefly, we first modeled an individual beam unit (40 µm L x 2000 µm W x 80 µm H) in Blender, and then duplicated the beam to form a planar array of beams with final lateral dimensions of 2000 µm × 2000 µm. To build out the full 3D structure, this planar array was then duplicated along the Z-direction using the same 40 µm spacing, in order to produce an array of beams that had the final dimensions of 2000 µm × 2000 µm × 4000 µm. The resulting array was subsequently duplicated and rotated twice more along orthogonal axes, and then the three arrays were overlayed on top of one another to form the final 3D grid architecture, which produced a porous structure with 40 µm pores, and 80 µm long channels (Figure 4).

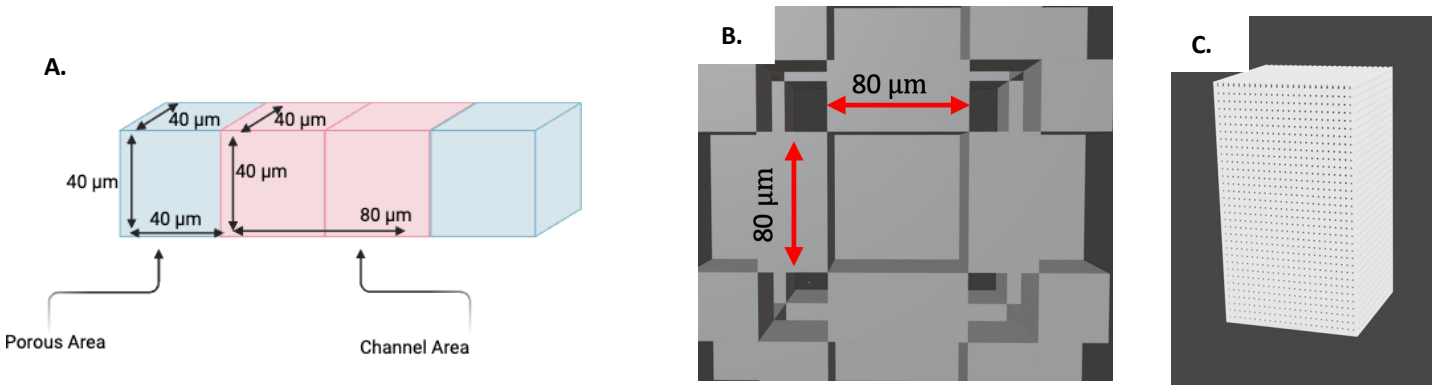

Figure 4A (left): *Schematic illustration of Porous Architecture B, and the dimensions of the porous areas and the channel area.* ***Figure 4B (middle):*** *Close up image of the truncated array of beams. As shown in the image, there is an 80 µm long channel between the pores.* ***Figure 4C (right):*** *Zoomed out image of the final grid structure. The final dimensions of the grid structure is 2000 µm L x 2000 µm W x 4000 µm H.*

2.2.3 Design and Modeling of Porous Architecture C

Finally, the same process described in section 2.2.1 was repeated to produce the Porous Architecture C design, which was a porous structure with 40 µm pores and 120 µm long rectangular channels in between two adjacent pores (Figure 5).

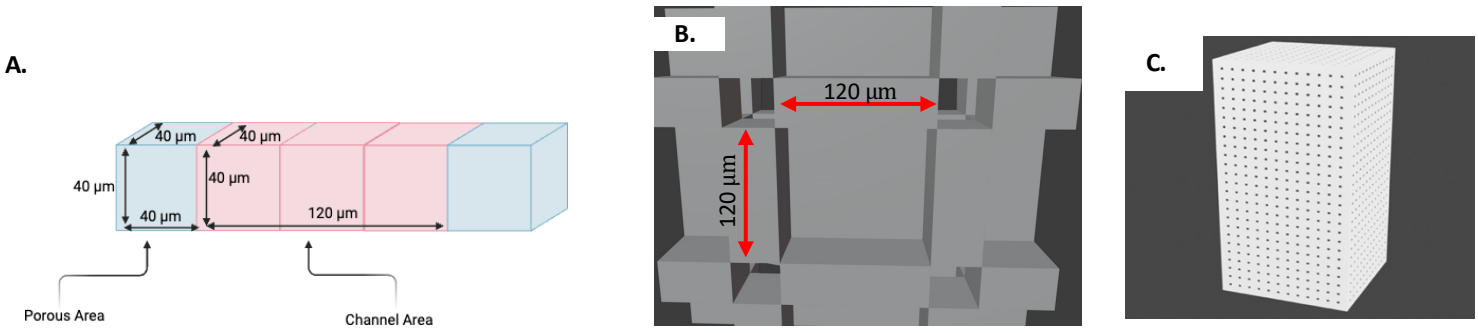

Figure 5A (left): *Schematic illustration of Porous Architecture B, and the dimensions of the porous areas and the channel area.* ***Figure 5B (middle):*** *Close up image of the truncated array of beams. As shown in the image, there is a 120 µm long channel between the pores.* ***Figure 5C (right):*** *Zoomed out image of the final grid structure. The final dimensions of the grid structure is 2000 µm L x 2000 µm W x 4000 µm H.*

2.2.4 Integration of Porous Architectures into a Cylindrical Configuration

A non-porous rectangular prism (2000 µm L x 2000 µm W x 4000 µm H) was generated in Blender. The three Porous Architectures previously built (Section 2.2.1-2.2.3) were then aligned into a grid formation, so that the top layers were all aligned at the same Z – position (Figure 6A, 6B and 6C). In subsequent iterations (Figure 6D), we opted to add a 40 µm wide non-porous wall in between all of the structures. The walls themselves were 2000 µm L x 40 µm W x 4000 µm H, and spanned in both the X and Y directions. Once the Porous Architectures were aligned, we then applied a Boolean modifier to each Porous Architectures, where a cylindrical wire shape (2000 µm in diameter, and 2880 µm in height) was the "Boolean object", and the operation was set to "intersect". In this

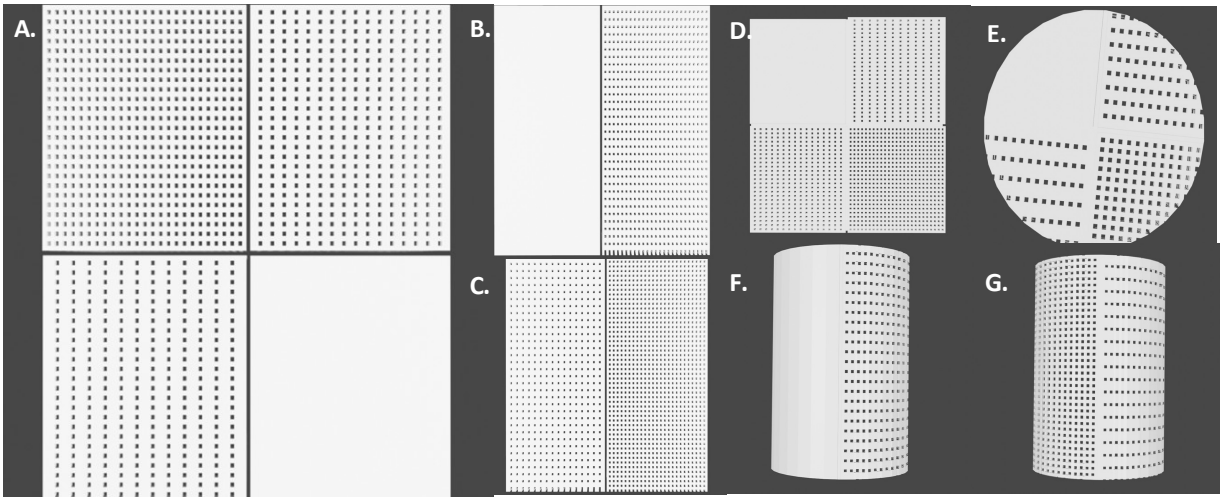

Figure 6*: Rendered final porous structure.* ***Figure 6A:*** *Top view of all of the assembled mesh structures aligned onto the grid. There was a 40 µm gap in between all of the structure.* ***Figure 6B and 6C****: Side view of the aligned mesh structures. The mesh structures were aligned so that top surfaces of the mesh structures were aligned to the same Z- position.* ***Figure 6D:*** *Top view of all of the assembled mesh structures aligned onto the grid, with the 40 µm wall inserted in between the different mesh / non-porous structures.* ***Figure 6E, 6F, 6G****: Top and side views of the structure post-Boolean modifier. The resulting structure was a porous cylinder with 3 different mesh structures, and one non-porous structure. The entire structure had a diameter of 2000 µm and a height of 2880 µm.*

fashion, each Porous Architecture was modified to leave behind only the sections that intersected with the cylindrical wire (Figure 6E, 6F, 6G). We elected to use a cylindrical shape as we initially planned to implant all scaffolds into the *bicep femoris* muscle area, and thus, the cylindrical design would've better assimilated with the muscle fibers in the area. Although we ultimately proceeded with a subcutaneous implant instead, we proceeded to keep the design as is, and assessed the performance of these scaffolds *in vivo*.

2.2.5 Additional Design Changes: Addition of the Sacrificial Support Structure(s)

Additional design changes were made in response to several challenges we faced during the printing process for the first and second versions of our scaffolds. In short, in order to counter some of the over polymerization and volume shrinkage issues, we opted to add a 1 mm non-porous cylindrical slab to the bottom of our porous structure, which also doubled as a "holding" unit for us to grab the printed structure with tweezers during the implantation surgery without damaging the porous area(s). Additionally, in order to better enable the rest of the structure to adhere to the moving stage, we opted to add a sacrificial support structure (200 μm thick) to the bottom of the non-porous cylindrical slab, as well as two 400 μm walls in an intersecting orientation to support the structure during the prints (Figure 7).

2.3 Acquiring Printable "Slices"

In order to print the design porous structure, the design was first transferred into printable slices (.lwo) using the 3D Slicer (Kloe, 3D Slicer Version 2.25.23) program, as described by Chen[52]. Briefly, the following steps were taken.

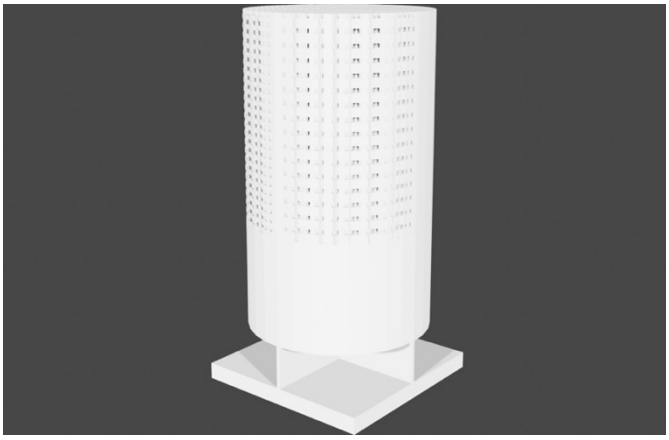

Figure 7: *Final porous structure containing all three mesh units with varying channel regions and 40 μm pores, as well as the sacrificial support structure, 200 μm base structure, and the 1 mm non-porous cylindrical slab attached at the bottom of the porous area.*

1. The 3D structure was exported as a .stl file, and opened using the 3D slicer software. The initialization point (the Z-position value where the printing stage touched the PDMS vat) was then entered as the "base height", and then the option to create an adhesion layer (base) was checked, along with the desired offset value and layer height. Finally, the writing direction was set to be "vertical".

2. On the next window, the desired slicing pitch (40 μm) was inputted.

3. On the next window, the option to "Attempt fixing the unclosed contours issues (RED)" was checked. This feature ensured that all the layers would print completely. Additionally, the contour option was checked off, and filling option was set to be vertical.

4. Finally, the desired values of start stabilization length, end stabilization length, laser modulation and writing velocity were all entered, and the printable slices were generated. In this case, the stabilizations lengths were set to .05 mm and the modulation and writing velocity were set to 100% and 60 mm/s.

5. Once the printable slices were generated, they were then imported into the KLOE Dilase 3D printer printing menu (KLOE Dilase 3D, KLOE).

2.4 Stereolithography 3D Printing

2.4.1 Sensitivity Test

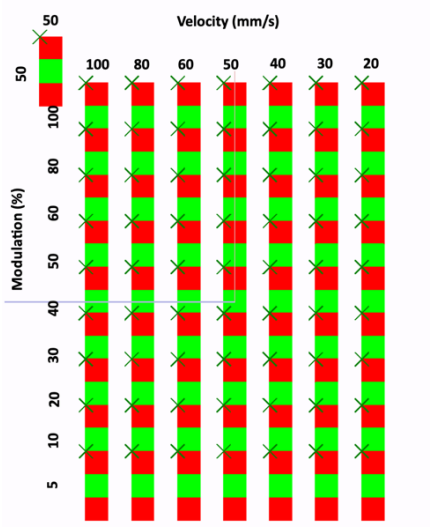

Figure 8: *Schematic illustration of sensitivity test. The green squares indicated when the laser is ON, and the red squares were where the laser is OFF.*

Upon completing the initialization process, as well as attaching a clean, pre-sanitized glass slide to bottom of the printing stage, the photosensitive 3D printing resin VITRA DS-2000 (DWS, Lot# 10200075) was added to the printing vat. The glass slide was used in order to preserve a smooth printing surface, as the printing stage was damaged in prior experiments[26, 51, 52].

Sensitivity testing was performed whenever the PDMS layer was freshly recoated, in order to evaluate the printing performance across a range of laser modulations and laser velocities. Here, the laser modulation refers to how often the laser is turned on and off during movement (a 20% modulation has the laser "on" 20% of the time, whereas an 80% modulation has the laser "on" 80% of the time), and the laser velocity refers to the speed the laser beam moves across the printing surface. The sensitivity test used a pre-developed test pattern by KLOE (Figure 8) containing 63 squares [100 µm × 100 µm (X, Y)], and each square was printed using a different printing modulation (100%, 80%, 60%, 50%, 40%, 30%, 20%, 10%, 5%) and laser velocity (100 mm/s, 80 mm/s, 60 mm/s, 50 mm/s, 40 mm/s, 30 mm/s, 20 mm/s). Once all squares had printed (as well as one reference square, which was printed using 15 mm/s velocity and 50% modulation), the glass slide containing the squares were removed from the printing stage, immersed in 70% isopropanol for 10 minutes to remove any residual resin, and then imaged using under a Bright Field Microscope (Carolina Biological Supply Company) to find the laser velocity and/or modulation value that produced the least amount of overcuring. The corresponding laser modulation and velocity values were then used to print any subsequent structures.

2.4.2 Focus Test

Following the sensitivity test, a new, clean glass slide was reattached to the printing vat, and the focus test was imported and performed. Briefly, the focus test printed 21 squares and one reference square that were all 100 µm × 100 µm (X, Y), and the distance between each adjacent squares was 100 µm (Figure 9). Each square was printed using the optimal modulation value and a writing velocity obtained from the sensitivity test, as well as a unique focus value ranging from -1.0 to 1.0, except for the reference square, which received a modulation value and writing velocity of 50% and 50 mm/s, and a focus value of -.3. The focus value here represents the Z-height where the UV laser is most "sharply" in focus. Once all of the squares finished printing, the glass slide was once again removed from the printing stage, immersed in 70% isopropanol for a minimum of 10 minutes, and then imaged under a microscope. The focus

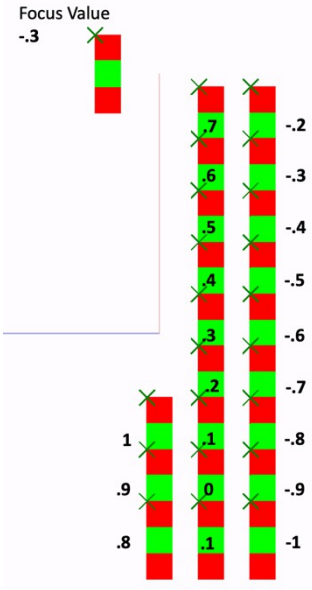

Figure 9: *Schematic illustration of focus test. The green squares indicated when the laser is ON, and the red squares were where the laser is OFF.*

value corresponding with the square containing the sharpest edges / corners was then selected, and this focus was used for all subsequent prints until the PDMS vat was recoated.

2.4.3 Recoating the Printing Vat with Polydimethylsiloxane

In order to preserve the printing quality, the printing vat was recoated periodically with a fresh layer of PDMS. Firstly, residual DS-2000 was removed by rinsing the printing vat with 70% isopropanol, and then the printing vat was disassembled in order to separate the PDMS layer from the rest of the vat. From there, the old PDMS layer was removed and then remaining printing vat, glass slide and tubing were all cleaned using 70% isopropanol to remove any leftover PDMS / DS-2000. Once the printing vat was cleaned, the vat was reassembled, and then ~12g of the Sylgard-184 silicone elastomer mixture consisting of a 10:1 ratio of base polymer to cross-linker was added to the bottom of the printing vat. This amount was selected in order to produce a PDMS layer around 22.6 - 22.8mm thick, which was the optimal thickness recommended by KLOE. The PDMS mixture was then left to solidify for 24 hours.

The PDMS vat was then subsequently stabilized, as described by Chen[26, 52]. Briefly, fresh DS-2000 resin was added to the printing vat and left for 120 hours. After 120 hours, the DS-2000 was removed from the printing vat and cleaned, before then being placed inside the UV Cross Linking Chamber (Spectro-UV, Spectrolinker XL-1500 UV Crosslinker) with 365 nm UV lights (BLE-1T151) for 9 minutes. This process was repeated once more, for a total of 2 stabilization processes. The stabilization process was used to mitigate internal contamination caused by resin absorption and subsequent photocuring within the PDMS substrate during repeated print cycles. This contamination altered the PDMS surface chemistry, resulting in inconsistent polymerization and poor layer adhesion. However, as discovered by Chen[26, 52], by following this stabilization process, we created a more inert and predictable surface, thereby improving printing consistency and precision in high-resolution SLA printing.

2.4.4 Fabricating the Porous Scaffolds

Once both sensitivity and focus test were completed, the desired printable files were imported, and the optimal laser modulation, velocity and focus values were entered into the printing menu. After the files printed, the resulting structures were immersed into 70% isopropanol to remove any excess uncured resin. The samples were then air dried at room temperature, and then the resulting print(s) were imaged using the SEM.

2.4.5 Measuring the Pore Sizes and Channel Sizes

To assess the pore sizes for each of the porous regions containing different channel ratios, we first imaged the pore size and channel regions using a top view and the cross sectional (side) view of the porous scaffolds under low magnification (200x). The average values for the pore size and channel regions were calculated using ImageJ. Pore / channel region size was calculated from SEM Images (n = 3 images), and for each image, 3 measurements were made. For some channel regions, the annotation feature was used to mark the edge of the pore to distinguish any areas where there was supposed to be a pore, but it was overcured / filled in.

2.5 SEM Imaging

SEM images were acquired on the printed samples and test specimens using either the sec SNE-3200M Scanning Electron Microscope (SEM) (SEC) or the Apreo-S/2S Scanning Electron Microscope (SEM) (Thermo Fisher Scientific) with an acceleration voltage at 2 kV or 5kV (depending on the SEM and tilting angle used). Only the outside contacting areas were measured for pore size and channel region size.

2.6 Cytotoxicity and Endotoxicity Testing

Cytotoxicity (MEM Elution Test) in compliance with ISO 10993-5 guidelines for the 3D printed scaffolds. Briefly, scaffolds were soaked for 24 hours in DMEM, and then the conditioned media was exposed to live L929 (Thermo Fisher Scientific) cells for 48 hours. After t=24 hours and t=48 hours, cells were assessed under visual microscopic inspection for any cells damage and graded for cytotoxicity using the standard provided in ISO 10993-5. Endotoxicity testing was performed as described in the manufacturer's protocol (PierceTM Chromogenic Endotoxin Quant Kit, Thermo Fisher Scientific). Prior to any testing, all scaffolds were washed in a serial ethanol dilution to remove any residual DS-2000 (Table 2). Ethanol solutions were changed every 2 hours, and once the scaffolds had been washed thrice at a given concentration, the scaffolds were then transferred to the next ethanol concentration in the series. Washed scaffolds were then rinsed thrice with deionized water, placed in 1X PBS, and then stored at 4 °C prior to testing.

***Table 2**: Ethanol wash cycles used prior to cytotoxicity and endotoxicity testing*

Wash Cycle	Ethanol Concentration
1	30% Ethanol (x3)
2	50% Ethanol (x3)
3	70% Ethanol (x3)
4	100% Ethanol (x3)
5	70% Ethanol (x3)
6	50% Ethanol (x3)
7	30% Ethanol (x3)

2.7 In vivo Animal Experiments

All animal experiments were approved by the University Animal Care and Use Committee (IACUC) and conducted in accordance with the National Institutes of Health guidelines for the care and use of laboratory animals. Six (n=6) male C57Bl/6 mice aged 10-12 weeks and weighing 20-25 g (Charles River) were used.

2.7.1 Subcutaneous Implantation Surgery

Mice were first anesthetized with 3-5% isoflurane inhalation and then given an injection of buprenorphine following a dosage of 0.05mg/kg to manage post-surgical pain management. Two crosswise incisions were then made in the left and right back regions, and the blunt end of a surgical scalpel was used to create a subcutaneous pocket on each side. Each pocket received a single randomized implant (Table 3), and the incisions were closed using wound clip and staples. Animals were monitored for any signs of discomfort, inflammation, or weight loss were observed over a 33-day period. Staples were removed 11 days after the implant date.

Two pHEMA discs with 100 µm pores were included as additional positive controls, and one pHEMA disc with 40 µm pores and one DS-2000 disc with 40 µm pores were also included as the negative controls. All control discs measured 5 mm in diameter and 1 mm, and were taken from a previously manufactured batch of scaffolds made using the patented bead sintering method[22, 24, 25, 35]. All scaffolds had been previously assessed for cytotoxicity and endotoxicity and passed[51].

***Table 3**: Implants used for subcutaneous surgery.*

	Mice Surgery Information	
Mouse Tag	**Right Side Implant**	**Left Side Implant**
A0	3D Printed Scaffolds	3D Printed Scaffolds
A1	3D Printed Scaffolds	3D Printed Scaffolds

A2	pHEMA 40 µm Punch out	pHEMA 100 µm Punchout
B0	3D Printed Scaffolds	3D Printed Scaffolds
B1	3D Printed Scaffolds	3D Printed Scaffolds
B2	DS-2000 40 µm Punchout	pHEMA 100 µm Punchout

2.7.2 Implant Harvesting and Processing for Histology

Following the 4-weeks, all mice were euthanized via cervical dislocation (due to the CO_2 chamber malfunctioning mid-experiment), except for one mice (A0), which was euthanized by CO_2, followed by cervical dislocation. Implants and surrounding tissue were then harvested using scalpels and surgical scissors, and immediately fixed in 10% formalin solution for 24-48 hours at room temperature with gentle agitation (Orbital Shaker 7744-08096). All tissue were prepped for further processing by using a 50% ethanol (~10 minutes) and a 70% ethanol (~30 minutes) wash. Subsequently, the implants were then dehydrated, cleared, and paraffin-infiltrated using a tissue processor (Shandon Citadel 2000), and then embedded in paraffin (KEDEE, KD-BM11 Tissue Embedding Center) to produce blocks with all scaffolds being orientated perpendicular to the future microtome sectioning blade.

Tissue samples were sectioned into 5 µm thick slices with a microtome (LEICA, HistoCore Biocut RM 2135), transferred to a vat containing deionized water (33 °C), and then placed onto a glass slide (Superfrost Plus) for histology analysis. The slides were then air dried, baked at 53 °C for 30 minutes, and then cooled before the deparaffinization process. For quantitative analyses, two or three sections, at least 120 µm apart, were collected on the same glass slide.

2.7.3 FBC Thickness Measurement

Masson's trichrome (Tyr Scientific, LOT # 80886) staining was performed on sectioned tissue following instructions from the manufactures. In order to quantify the fibrotic capsule thickness for all explants, a perpendicular line was drawn from the interface of the capsule and to the approximate outer surface of the fibrotic capsule for the high magnification images obtained (20x) and then the distances was calculated using the scale bar associated with each image. In order to reduce variability, capsule thickness measurements were made only in implants sections with minimal to zero adipose encasement. Six random measurements per section were made and averaged, and for each explant, three sectioned were analyzed.

2.7.4 H&E Analysis for Cellularization

H&E staining (Sigma-Aldrich, LOT # SLBT4556, LOT# SLCC8965) was performed following the manufacturer's protocol. The stained tissue was analyzed under high magnification (20x), and for each implant, at least one section was selected for analysis. For each section analyzed, three random regions of interest were selected, and then the area of this region was measured using ImageJ and the associated scale bar. Subsequently, the number of nuclei within this region was counted, and then the cell density was calculated as the number of nuclei per unit area.

2.7.5 Histology Analysis

The stained tissue samples were imaged using a Nikon TE200 Inverted Microscope. For each tissue section, images were taken at the following magnifications: 4x, 10x and 20x. For each image, there were two versions saved: one with a scale bar and one without.

2.8 In Vitro Cellularization Experiments

Lastly, an *in vitro* cellularization experiment was conducted following the animal experiments in order to better understand the cellularization behavior observed. Three (n=3) of each scaffold type (DS-2000, pHEMA 40 µm, pHEMA 100 µm and 3-D printed) scaffolds were rinsed using 70% ethanol thrice, and then coated with Poly-D-lysine (Gibco, LOT# 1569787) for 1 hour under gentle agitation. The scaffolds were then placed into a 48 well plate, and then 1.5 mL of 3T3 cells (1 x 10^5 cells / mL) were seeded on top of each scaffold. The cells and scaffolds were the incubated at 37°C for 48 hours.

2.8.1 In Vitro Cellularization Analysis

Following the 48-hour incubation period, the scaffolds were transferred to a fresh 12 well plate, and then fixed with 2mL of Karnovsky's solution (Electron Microscopy Solutions, LOT#220114-07) for 2 hours at room temperature. The scaffolds were then rinsed with a calcium carbonate solution, stained using osmium tetroxide (Electron Microscopy Solutions, LOT#221219-19), rinsed once more with calcium carbonate solution and then dehydrated in a series of ethanol rinses, starting with 70% ethanol and going all the way to 100% ethanol. The samples were then dried in the CPD chamber (Denton DCP-1), sputter coated with platinum (Leica ACE600), and then imaged under SEM to assess for cell infiltration (Apreo S/2S SEM).

2.9 Data Analysis

2.9.1 Statistical Analysis for the Pore Sizes and Channel Region Measurements

To assess whether the orientation of pore size measurement affected observed values, average pore sizes in the X-direction and Z-direction were compared against one another across all porous layers using a paired t-test. For each porous layer, triplicate values were obtained from three distinct regions and averaged separately by direction, and normality was assessed using Shapiro-Wilk test. For approximately normal data, a paired t-test was used to compare matched pore size values in the X and Z directions across the same porous layers, whereas a Wilcoxon signed-rank test was used for all other data sets.

Finally, in order to assess whether the pore size measurements made differed significantly across the three Porous Architectures (A, B, and C), a one-way ANOVA test, followed by Tukey's Honest Significant Difference (HSD) post-hoc test to determine which specific architecture pairs differed. For datasets that violated normality assumptions, the Kruskal-Wallis test, followed pairwise Mann-Whitney U tests with Bonferroni correction was performed. For all assessments, an p-value of 0.05 was used to determine statistical significance. This same process was repeated for the channel region measurements.

2.9.2 Statistical Analysis for Foreign Body Reaction Assessment

A one-way ANOVA test was used to assess for statistical differences in the fibrotic capsule thickness and cell density measurements made across the different porous architectures and the various control groups, and a Tukey's post hoc analysis was completed to evaluate statistical differences if the ANOVA test yielded significant differences. The significance levels of the statistical results were all $p < 0.05$.

Chapter 3: Results and Discussion

3.1 Sensitivity Test

The results from the sensitivity test completed prior to printing the first iteration, second iteration and third iteration are shown below (Figure 10). For each of these sensitivity tests performed, there were more than 40 squares printed, which indicated that the PDMS had cured and stabilized properly, and thus, we could proceed with the next tests / prints. We also observed that the squares with the least deformation were found with lower laser modulation and laser velocity settings, and this, combined with historical data from prior printing runs[26, 51, 52] led us to target a laser modulation somewhere in between 30% and 40%, and a laser velocity from 40% to 70% for all future print.

Interestingly, we also noticed that after we used the printed for an extended period (~20 prints), the desired structures would no longer be produced, and instead, we only observed the first few layers of the structures floating in the resin. We believed this happened due to the conditions of the PDMS layer changing (as explained by Chen[26, 52]), the laser modulation that was previously used was no longer strong enough to fully polymerize the structure, and as a result, the structures subsequently failed to adhere to the printing stage. We later confirmed this by printing the sensitivity test after ~20 prints, where we observed that only 15 squares printed (Figure 10D). Although in theory we could've attempted to print the 3D scaffolds using a higher laser modulation and velocity values, we opted to instead recoat the PDMS and use fresh DS-2000 resin, in order to have more control over the printing settings. Moreover, these results confirmed that even with the stabilization process, the PDMS performance continued to change, and thus, in order to maintain batch to batch consistency and overall printing quality, we elected to reduce the number of prints made per each PDMS layer to no more than 15 structures, or until the squares at 30% modulation could no longer be printed (whichever came first).

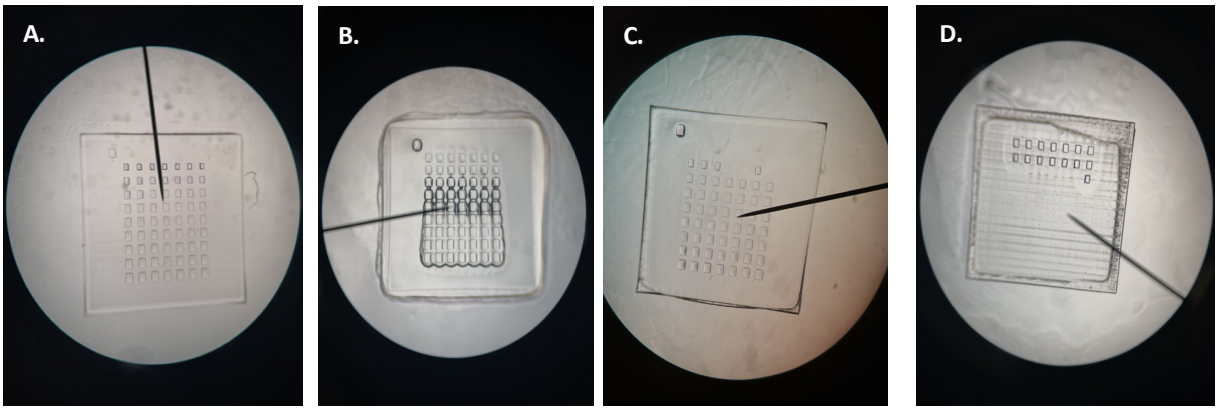

Figure 10: *Sensitivity test results.* ***Figure 10A:*** *First sensitivity test completed before the first designs were printed.* ***Figure 10B:*** *Sensitivity test results prior to the second design being printed.* ***Figure 10C:*** *Sensitivity test results prior to the third designs being printed* ***Figure 10D:*** *Sensitivity test completed after the first designs were printed. There was only 15 squares printed, which indicated that the PDMS needed to be recoated*

3.2 Focus Test

The results of the focus test completed prior to printing the first iteration, second iteration and third iteration are shown below (Figure 11). We observed here that the optimal focus values changed each time the

PDMS vat was recoated, where the first focus test yielded an optimal focus value of -.3 but for the second and third times, the ideal focus value was -.6. We attribute these difference in focus values to the deviations in the thickness of the PDMS vats. More specifically, as the focus value was effectively a measurement of the vertical (Z-axis) position of the stage or objective, in a thicker PDMS film, in order to compensate and maintain the same relative focal point at the resin surface, the stage must be translated further down the Z-axis, which thus resulted in a more negative focus value. Fortunately, as was by confirmed by Chen[26, 52], it was possible to produce porous scaffolds with the same printing quality across different focus values, but it required additional fine-tuning of the laser modulation / velocity settings to optimize the printing settings. Furthermore, unlike the sensitivity test, Chen also determined that the focus value didn't change over time like the sensitivity test results; thus, the same focus value could be used for all subsequent prints, until the PDMS layer was eventually recoated.

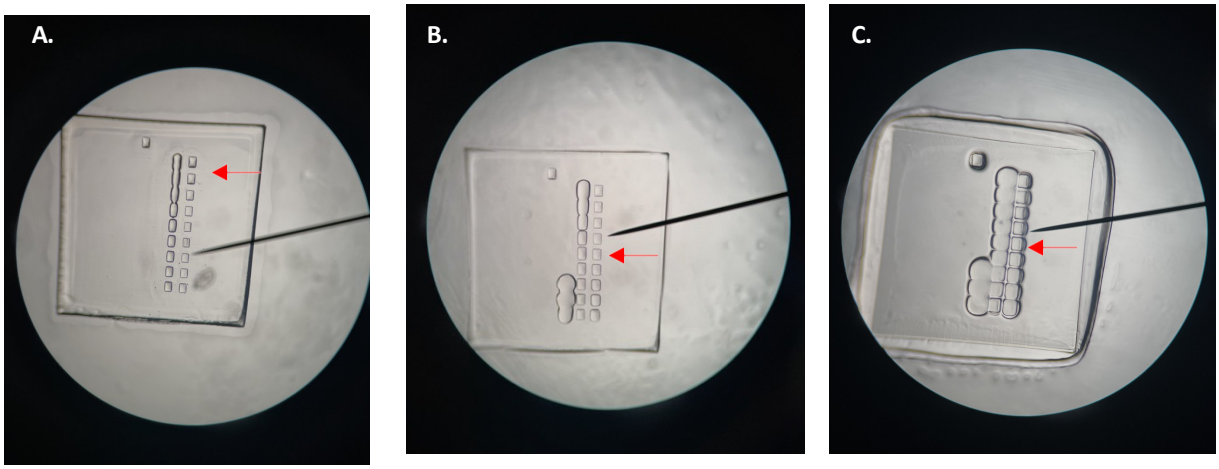

***Figure 11**: Focus test results. The squares highlighted by the red arrow were the focus values chosen for each focus test **Figure 11A:** First focus test completed before the first designs were printed (Focus Value -.3). **Figure 11B:** Focus test completed prior to printing the second designs (Focus Value -.6). **Figure 11C:** Focus test results prior to the third design being printed (Focus Value -.6).*

3.3 First Printing Attempts of the Varying Multi-Channel Scaffolds with the 40 µM Porous Units

Initially, only 20 layers of the designed porous structures were printed as a proof-of-concept, using the following printing settings: 40% modulation, 50 mm/s velocity, and a focus value of -.3. In total, the entire structure took 27 minutes and 40 seconds to print, and the resulting structure was washed in 70% isopropanol for another 30 minutes. As indicated in Figure 12A, the printed scaffold properly displayed all four Porous

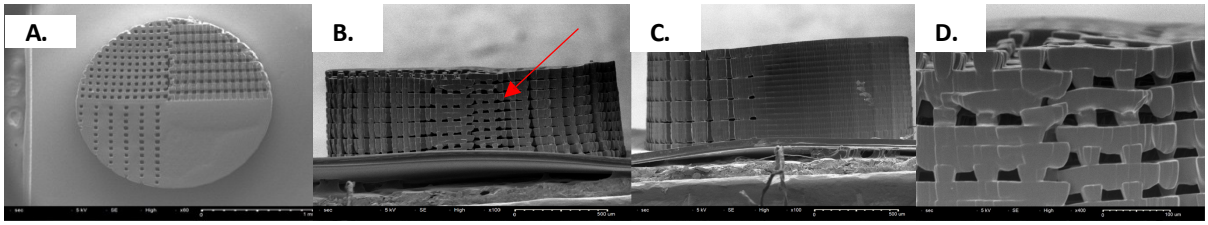

***Figure 12A:** SEM images of the top view of the fabricated preliminary porous scaffolds. **Figure 12B and Figure 12C**: SEM images of the side view of the fabricated preliminary porous scaffolds. On the left side is Porous Architecture A & B, and on the right side is the 1 Porous Architecture C & D. The intersecting point between the Porous Architecture A & B is highlighted by the red arrow, and was indicative of a poor transition between the two units, which resulted in the jagged print produced. **Figure 12D**: Zoomed in image of the transition between Porous Architecture A and B*

Architectures, and the top view properly showcased the successful fabrication of both the pores and the channel region. Furthermore, subsequent analysis in ImageJ showed that across the top view, the average pore size for all Porous Architectures fell within the desired range of 30 µm to 40 µm, and the diameter of the resulting scaffolds were 1.75 mm (side to side) and 1.68 mm (top to bottom). However, when we analyzed the cross-sectional view (Figure 12B), we observed that visually, the pores were more profoundly occluded in the Z-direction compared to the X-direction. This prompted us to measure the pore size measurements in both the X-direction and the Z-direction, in an effort to accurately capture the pore sizes.

Indeed, as shown in Figure 13, across most of the layers, the average pore size measured in the X-direction was much larger than the average pore size in the Z-direction, and furthermore, for most of these layers, those differences were statistically significant as well. We hypothesized this behavior was due to a combination of the overcuring and volume shrinkage behavior observed by Chen[26, 52] (discussed in depth in below sections), and as such, elected to reduce the laser modulation for future prints in order to combat this behavior. Lastly, we also noted that the transition between Porous Architecture A and B was poor, which resulted in the jagged, misaligned region highlighted in Figure 12B and Figure 12D. Out of concern of potentially exacerbating the foreign body response, we also elected to add a 40 µm walls in between all Porous Architectures in order to better blend the transition between each Porous Architecture.

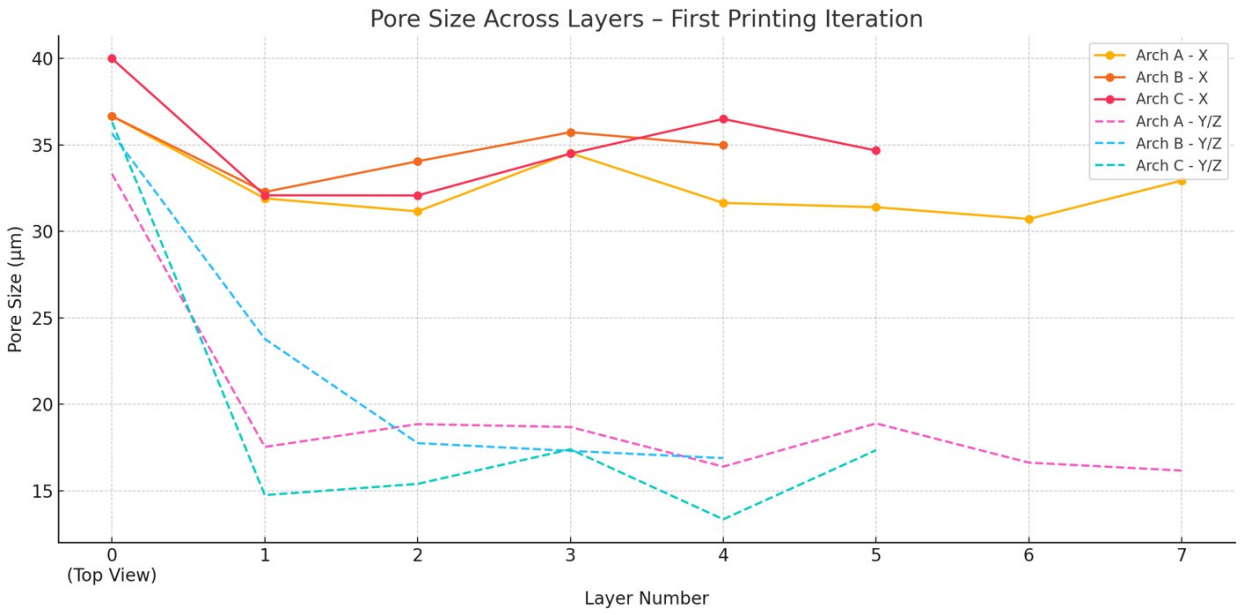

Figure 13: *Analysis of pore size for the first iteration of the printed scaffolds. Layer 0 was the top view (measurements made in the X and Y direction), and the Layer 1 – Layer 7 were the porous layers that followed (measurements made in the X and Z-direction). As shown, the Z-direction measurements were much smaller than the X-direction measurements across Layer 1 – Layer 7, which indicated that there may have been extensive overcuring.*

3.4 Second Printing Attempts of the Multi-Channel Scaffolds with the 40 µm Porous Units

Once the aforementioned design changes were made, we proceeded to print the full structure (68 layers) using the following printing settings: 37% modulation value, 50 mm/s velocity, and -.6 focus value. After these scaffolds were printed, they were rinsed in 70% isopropanol for 24 hours, and then SEM images of these structures were taken. As showcased in Figure 14A, the printed scaffold properly displayed all four Porous Architectures, and once again, the top view properly showcased the successful fabrication of both the pores and the channel region in the desired pore size range (average pore size value in Porous Architecture A, B, and C, were 36.2 $\pm$ 4.26 µm, 38.4 $\pm$ 6.09 µm and 31.4 $\pm$ 1.95 µm, respectively). However, further examination of the cross-section views indicated that the bottom layers of the scaffolds were all over-cured, and warped together to form a large over-cured "bump" structure (Figure 14B). While the "bump" structure could be removed using a razor blade, we also noted that all of the pores were occluded on the bottom layer (Figure 14C), which was undesired, given that the non-porous nature would prevent cell infiltration, etc.

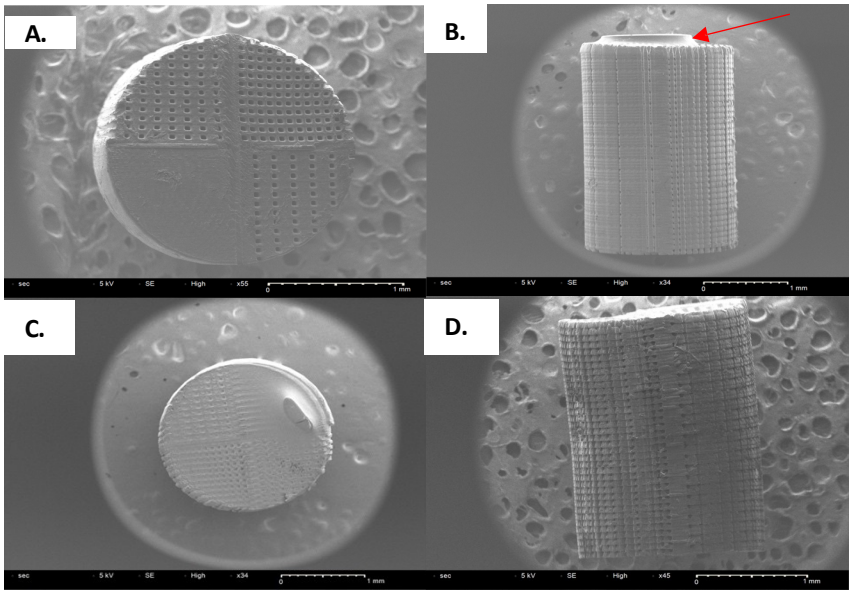

Figure 14A: *Top view of the fabricated second iteration of the porous scaffold.* ***Figure 14B:*** *Side view of the fabricated second iteration of the porous scaffolds. The raised bump (highlighted by the red arrow) observed at the top of the scaffold is the non-porous structure that is most likely the result of those layers overcuring and simultaneously shrinking together.* ***Figure 14C:*** *Bottom view of the fabricated scaffolds. The raised bump observed on the right side of the scaffold is the same structure observed in Figure 14B. As seen in the image, the pores on the bottom layer of the porous scaffold are filled, which indicates that the bottom layer overcured heavily.* ***Figure 14D:*** *Side view of the fabricated scaffold.*

Further, when we assessed the pore sizes using ImageJ, we noticed that the pore measurements made in the Z-direction were once again much smaller compared to the X-direction across all Porous Architectures. Although additional statistical analysis demonstrated that these differences were not statistically significant (Table 4) (likely due to the low sample size and high variability among the pore size measurements), we observed that on average, there was ~30% reduction in pore sizes when we compared the measurements made in the X versus Z direction for Porous Architecture A, ~20% reduction when we compared the measurements made in the X direction versus Z direction for Porous Architecture B and ~8% reduction when we compared the measurements made in the X direction versus Z direction for Porous Architecture C (Figure 15). While some of these differences are attributed to natural error caused from the measurement process, we believed that it was highly unlikely that error alone caused these discrepancies in pore size, which indicated that

Table 4: *Summary of the statistical calculations performed to compare pore size measurements made in the X versus Z-directions*

Porous Architecture	Paired T-Test Sig. (X vs Z)	Wilcoxon Sig. (X vs Z)	Total Comparisons	% T-Test Significant	% Wilcoxon Significant
A	1	0	19	5.263157895	0
B	3	0	19	15.78947368	0
C	0	0	9	0	0

additional considerations were required to further optimize the printing quality and ensure uniformity across both X and Z axes.

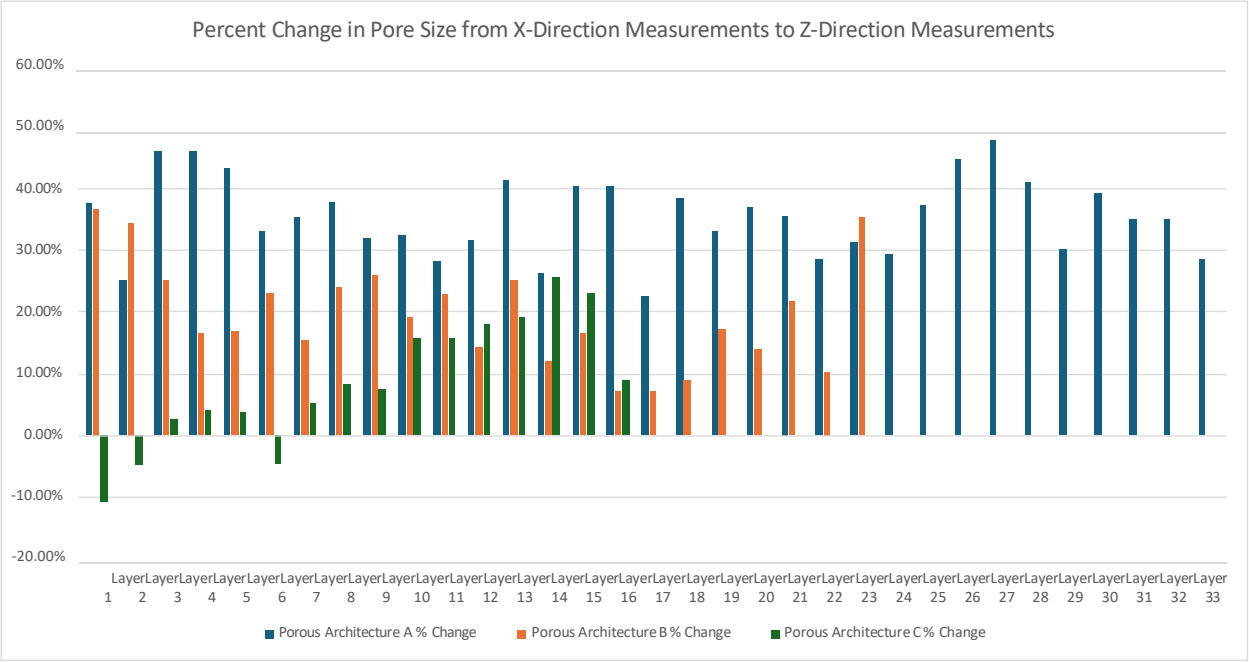

Figure 15: *Percent Change in Pore Size Measurements Made across the X-Axis and the Z-Axis*

One possible explanation for this behavior was improper resin drainage. More specifically, although the design of the scaffold should've permitted resin drainage in all directions, there likely was insufficient vibration / agitation during the print to remove the resin from the porous scaffolds prior to the next layer being polymerized, especially given the high viscosity of DS-2000. Moreover, due to the influence of gravity, more resin may have pooled and become trapped within the pores along the Z-axis. This trapped resin likely underwent partial curing, either from scattered UV light or secondary curing from the UV light, which partially explains the observed discrepancies in pore size measurements between the X- and Z-directions.

However, we also believed that our scaffolds encountered a phenomenon known as "volume shrinkage" (or axial shrinkage), which was evidenced by the diameters of the fabricated scaffold measuring 1.853 mm (X) x 1.861 mm (Y) in the top view instead of the original 2 mm (X) x 2 mm (Y) dimensions. Many others have documented a similar behavior, where they observed ~10-20% shrinkage[63-65] in their designs, although the extent of the shrinkage behavior widely varies on the material type and the 3D printing technique. However, recent research has also shown that volume shrinkage may also occur during the washing / drying process, where the capillary forces from the drying alcohols within the porous structures may induce structural collapse and/or additional contraction, which thereby leads to reduced pore sizes[63, 66-70]. Moreover, as observed by Liu et al., this shrinking behavior may not be uniform, and in some situations, scaffolds may have higher shrinkage rate in the Z direction compared to the X and Y directions[71], as was also observed by Park et al. [66], Arora et al.[67] and Denis et al.[72]. This volume shrinkage behavior better helps explains the overall reduction in pore size we observed, as the majority of the pore size measurements yielded values that were below the intended 40 µm size.

Despite these issues, the best way to minimize the effects of resin drainage and volume shrinking with the DS-2000 resin were to continue modulating the printing settings, as was described by Chen et al.[26, 52] However, we also theorized that the warping behavior observed in the bottom layer was potentially due to a poor adhesion of the printed structures to the surface of the glass, and thus, we hypothesized that with additional design

modifications, we could control the extent of this behavior. Although other strategies, such as coating the glass slide with adhesive materials were explored, ultimately, we added the "sacrificial support" structure described in above sections, in hopes to increase the adhesion and mitigate the likelihood of the structures warping inwards, and then proceeded to print the new structure with a reduced modulation / increased velocity.

3.5 Final Print of the Multi-Channel Scaffolds with the 40 μm Porous Units

The newly designed porous structure (from Section 2.2.5) was printed using a final laser modulation of 35%, velocity of 60 mm/s, and a focus value of -.6. In total, it took 2 hours and 10 minutes to print all 107 layers, and once the structure finished printing, the scaffolds were immersed in 70% isopropanol alcohol for 72 hours to remove any residual resin. We first confirmed the successful fabrication of the sacrificial support structure using a microscope (Figure 16), and observed that the inclusion of the sacrificial scaffold and the non-porous cylindrical slab had worked well to contain the volume shrinkage (warping) behavior previously observed to the gap region in between the support structure and the non-porous slab, which was easily removed using a razor blade.

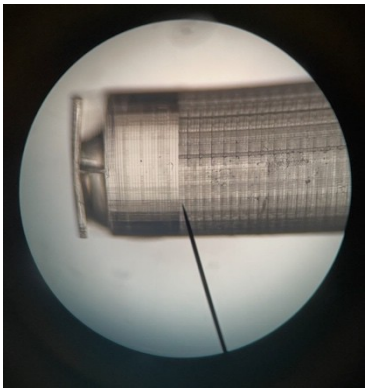

Figure 16: *Image (10x) of the porous scaffold with the sacrificial support structure (left most structure), and the non-porous cylindrical slab.*

3.6 Analysis of Pore Size and Channel Region Thicknesses

3.6.1 Top View Pore Size Analysis

Subsequent analysis of the fabricated scaffolds in ImageJ showcased that the average pore sizes of the top surface was slightly below the desired 40 μm pore size across all Porous Architectures (Table 5), but was well within the desired the 30 μm – 40 μm pore size range. Moreover, through additional statistical analyses, we observed that there was no statistical difference between the mean pore size made in the X-direction and the Y-direction for all Porous Architectures (p-value from paired t-test for Porous Architecture A = .073, Porous Architecture B = .112, and Porous Architecture C = .070), which suggested that the slight deviations observed in the pore size were most likely due to how the measurements were made in ImageJ.

Table 5: *Pore size measurements of the top layer for each of the porous units. Each value shown in the table was the average value of three random pore size measurements made in ImageJ, for three different samples.*

Average Pore Size (Top View)		
	Mean Length X - Direction	**Mean Length Y-Direction**
Porous Architecture A	$30.51 \pm .79$ μm	33.76 ± 2.19 μm
Porous Architecture B	30.90 ± 1.69 μm	33.33 ± 2.79 μm
Porous Architecture C	32.19 ± 1.73 μm	$35.45 \pm .65$ μm

3.6.2 Cross Sectional Pore Size Region Analysis

Likewise, while the cross-sectional pore size measurements demonstrated that the pore sizes across all Porous Architectures were slightly below the desired 40 μm pore size, we observed that the majority of pore size measurements were within the desired the 30 μm – 40 μm pore size range as well. Moreover, whereas in the prior printing iterations we had observed a noticeable difference in the pore measurements made in the X-direction versus the Z-direction, here, there was a strong consistency between the pore measurements made in X and Z

axes (Figure 17), which demonstrated that the addition of the support structure had greatly improved the overall consistency in pore size produced.

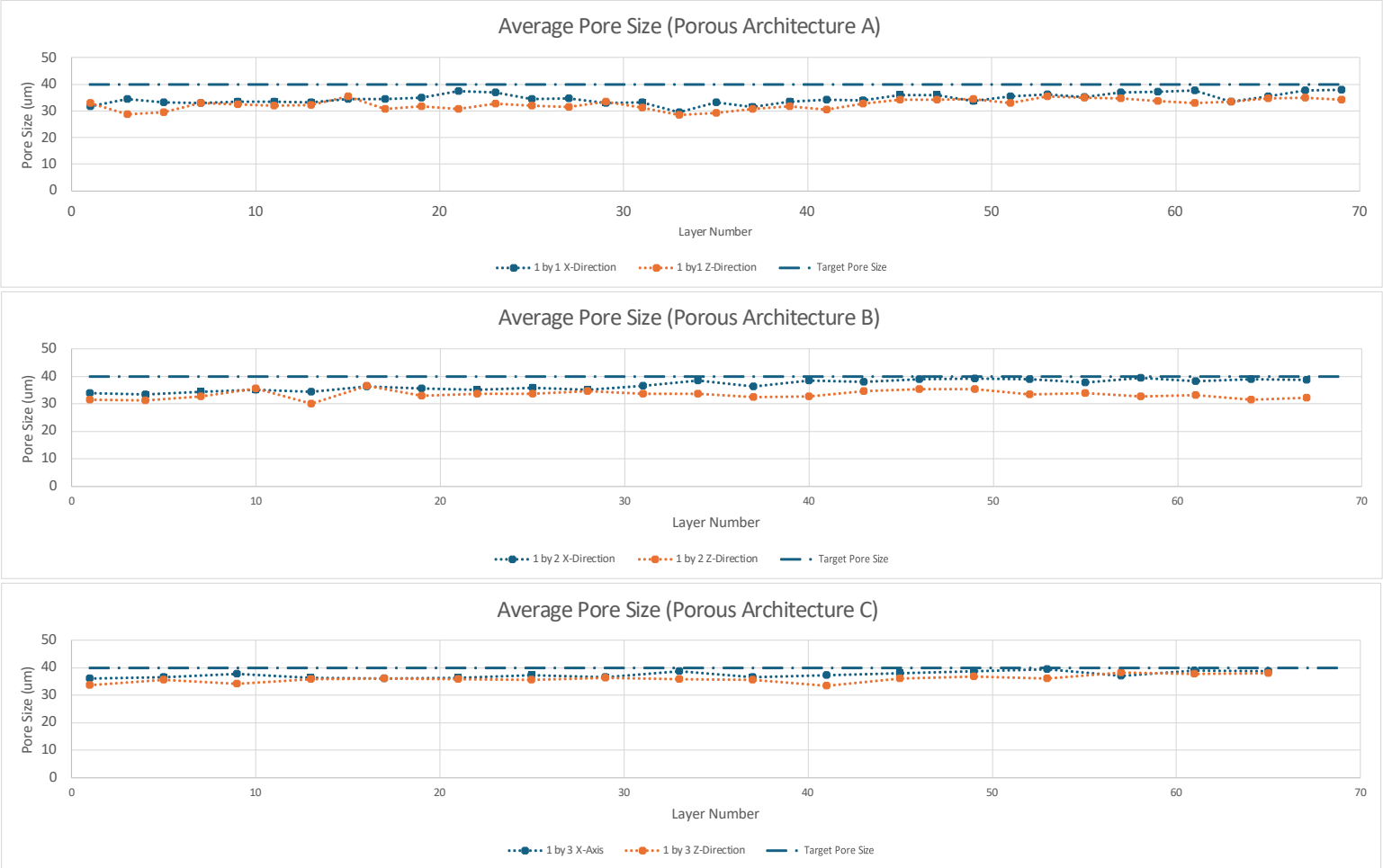

Figure 17: *Pore measurements of the final printed structure across all porous units. The dashed blue line highlights the ideal pore size (40 µm), and each data point represented an average of three pore size measurements taken for their respective layer number*

We then assessed whether there was a statistical difference in the average pore size measurements made across the X-direction and Z-directions for the cross-sectional analyses, and with the exception of a few layers, there was no statistical difference between the pore sizes in the X and Z-axis across all Porous Architectures (Supplementary Table 1, 2 and 3). Subsequent analysis to assess whether there was a statistical difference in the average pore size measurements made across the different porous architectures indicated that in both the X and Z-directions, there was a significant difference in pore size across the three Porous Architectures ($p < 0.001$), and subsequent post-hoc analyses indicated that Porous Architecture A had significantly smaller pore sizes than both B and C, although there was no significant difference in pore size across Porous Architecture B and C in the X-direction).

These results showcased that the effects of volume shrinkage and resin drainage / overcuring were still apparent despite the additional design modifications made, and to some extent, indicated that these effects were difficult to fully eliminate without making additional radical changes to the design, or utilize less viscous printing resins, etc. However, the significant improvements made from the previous printing attempts confirmed that the addition of the sacrificial structure had helped improve overall consistency across all porous layers, and the ability to produce these multi-design porous structures with 30 μm – 40 μm pores consistently in one consecutive print will inevitably help advance the capabilities of our research group towards producing more sophisticated designs.

Table 6A (top): *Statistical Testing completed to assess significant differences in pore size measurements across different porous architectures.*
Table 6B (bottom): *Post-hoc analysis completed to determine which porous architectures had statistically significant differences in pore sizes*

X-direction Test	X-direction Statistic	X-direction P-value	Z-direction Test	Z-direction Statistic	Z-direction P-value
ANOVA	33.38980088	2.10E-13	**Kruskal-Wallis**	21.23007165	2.45E-05

Porous Architecture 1	Porous Architecture 2	Tukeys HSD P-Value (adj.)	Mann U P-Value (adj.)
A	B	0.000	0.326
A	C	0.000	0.006
B	C	0.594	0.000

3.6.3 Top View and Cross-Sectional Channel Thickness Analysis

The channel region measurements were first assessed using the top view. The average channel sizes on the top surface was slightly below the desired lengths across all Porous Architectures (Table 7), which likely was from the volume shrinkage behavior explained earlier.

However, as shown in Figure 18, across each of layers printed in all Porous Architectures, while the channel regions were just under the desired thicknesses, there was excellent consistency in maintaining the desired channel size. Further statistical analysis to assess whether the channel measurements made in the X-direction versus the Z-direction were statistically different demonstrated that there was overall no statistical difference between the channel region measurements made across X-axis and Z-axis measurements (Supplementary Table 4, 5, 6). Indeed, once we graphed the channel region measurements, we noticed a frequent overlap in channel region measurements made across the X and Z-direction overlap frequently (Supplementary Figure 1), which showcased the overall success in producing porous scaffolds that had the desired range channel regions with low variability across all the layers in all Porous Architectures.

Table 7: *Channel size measurements of the top layer for each of the porous units. Each value shown in the table is the average value, taken from random 3 channel size measurements that were made in ImageJ.*

Average Channel Size	
	Mean Channel Length
Porous Architecture A	35.55 ± 2.85 μm
Porous Architecture B	68.82 ± 3.13 μm
Porous Architecture C	104.34 ± 3.10 μm

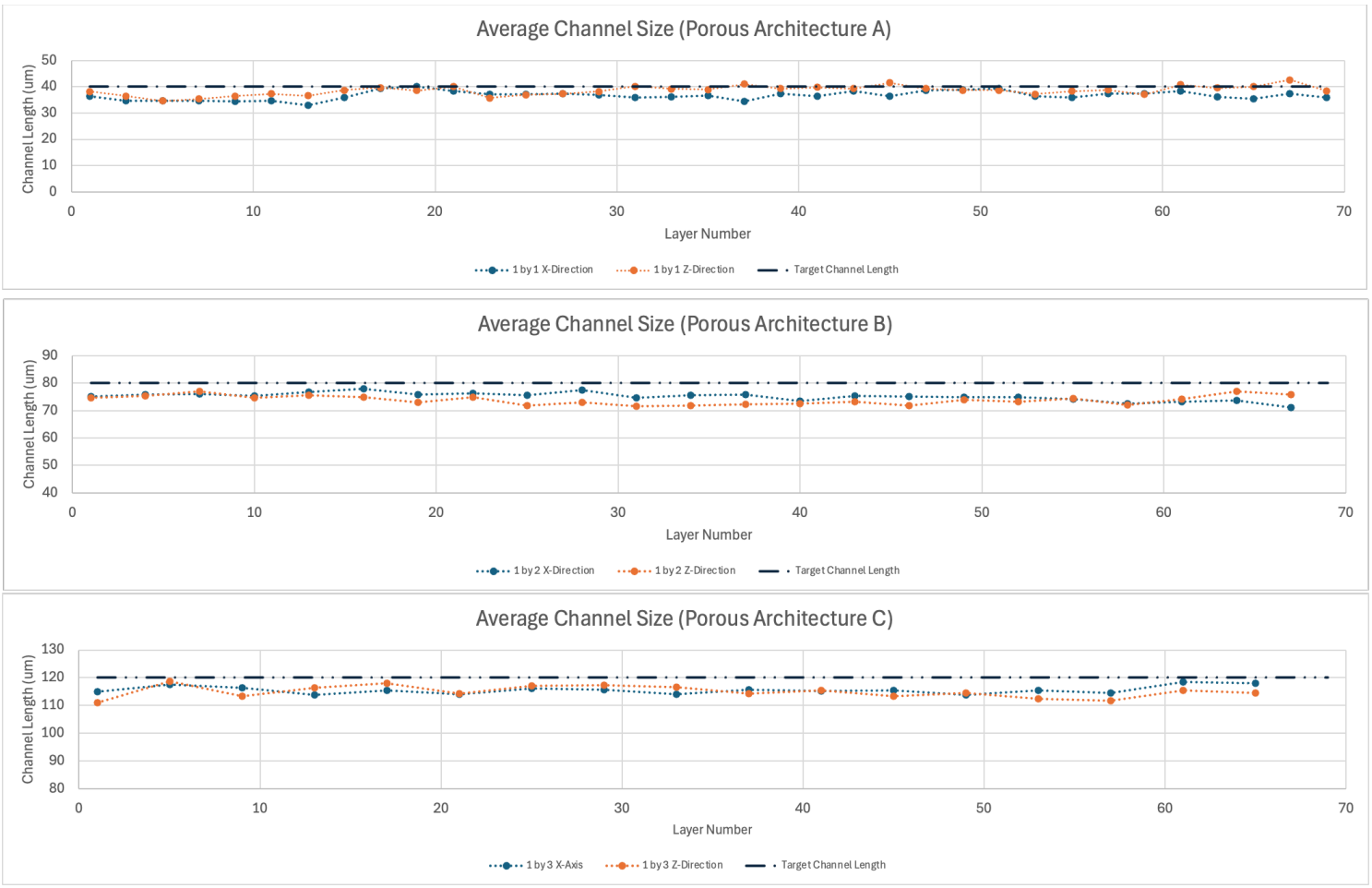

Figure 18: *Channel measurements of the final printed structure across all porous units. The dashed blue line highlights the ideal channel sizes (40 μm, 80 μm and 120 μm for Porous Architecture A, B and C, respectively), and each data point represented an average of three channel size measurements made for each respective layer number.*

3.6.4 Additional Considerations / Challenges

Separately, during the pore size / channel region measurements, there were several instances where it was difficult to accurately measure the true size, partially due to some overcuring, but also due to a minor design flaw. More specifically, as shown in Figure 19A, occasionally, the outside structure of the porous areas had unconnected "ridges", which occluded the pores. While these ridges (also known as boundary artifacts) shouldn't have impacted the ability of the macrophage cells to move into the scaffold (so long as the other areas were porous), they partially prevented us from being able to make accurate measurements of the pore and the channel regions, as there was one big open area instead of the siloed pore / channel region.

We attribute these ridges to the differences in how our structures were rendered in Blender versus how they were rendered and sliced in the 3D Slicer software. In short, although we observed in Blender that our porous scaffolds had clear edges and cubical, isolated porous units all the along the outer surfaces, when these structures were then rendered in the 3D Slicer software, there most likely was a misalignment (perhaps due to resolution limits), and the slicing software outputted sliced files that failed to fully capture the edges of the (Figure 19B). As a result, this led to partially generated cubical pores on the outside layers, which likely then overcured together to form the ridges we observed in some sections. Although we mitigated the extent of this issue by tilting the

structure during the SEM imaging, had we been able to, it would've been it better to modify the design so that the pores on the outer layer were perfectly cubical in the sliced designs in order to prevent this issue from impacting

Unfortunately, around this time, we began to notice that the performance of the printer was inconsistent, and more specifically, observed that most sensitivity tests failed to produce more than ~20-25 squares using the same laser modulation and laser velocity range as before, and on the few tests that yielded more than 40 squares, when we attempted to print the first few layers (which was the base unit + the sacrificial support structure), we observed that each layer was being printed slightly offset to the previous layer, which resulted in a sacrificial structured that was leaning over to one side (Supplementary Figure 2). Although further troubleshooting was required to diagnose the root cause, we believed that there likely was some misalignment in the optical path and/or a reduction in the laser power, and given the inability to successfully printed any more structures, we elected to proceed with the remaining experiment, albeit with a much smaller sample size than what we previously hoped to use (n = 12 scaffolds).

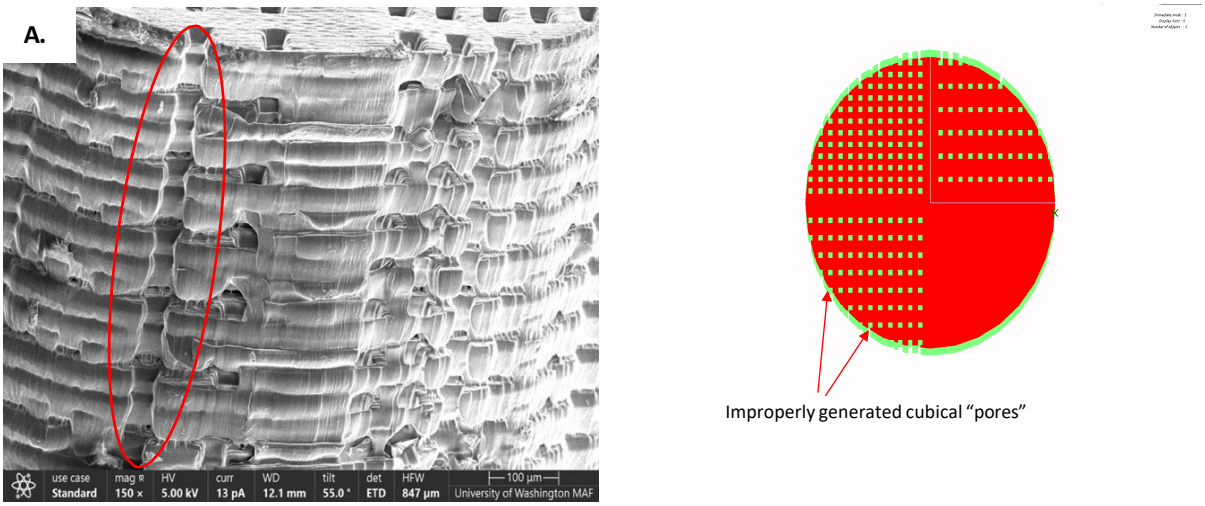

Figure 19A : *Boundary Artifacts ("Ridges") in the porous scaffold where there should've been porous units.* ***Figure 19B:*** *Schematic illustration of "design flaw". The generated sliced file should've contained fully generated cubes with all 6 side intact in order to minimize any possibilities of a partially printed structure, but instead, produced these "clippings", where the geometry was cut off improperly.*

3.7 Cytotoxicity and Endotoxicity Results

Six (n=6) of the 3D printed scaffolds, as well as three positive control samples (latex) and three negative samples (blank wells), were assessed for cytotoxicity testing. After 24 hours and 48 hours, the cell monolayers for each sample were assessed and scored according to ISO 10993-5 for cellular destruction (Table 8). As shown in Figure 20A, all of 3D printed samples had an average score below "1", which indicated that these scaffolds elicited slight damage to the cells after 48 hours. However, given that a numerical score of 2 is considered a cytotoxic effect, we determined that all of the tested implants had passed the cytotoxicity test, and were safe for use in future animal experiments. Similarly, endotoxicity testing was completed for three (n=3) of the 3D printed scaffolds (designated as 24h, 72h and 72h.2). After 24 hours, the endotoxin levels were measured, and as indicated below, all samples passed the endotoxicity testing (the maximum level for endotoxin is .06 EU/mL) (Figure 20B). As such, we proceeded with the animal experiments

***Table 8**: Cytotoxicity scoring metric, as defined in ISO-10993-5. The table quantifies the degree of cellular damage or reactivity under microscopic examination*

Grade	Reactivity	Condition of Culture
0	None	No cells showing damage, intracellular granulation, no cell lysis
1	Slight	<25% damaged cells (these cells are around without intracellular granulation occasionally cell lysis)
2	Mild	25-50% damaged cells (these cells are round without intracellular granulation) cell lysis
3	Moderate	50-75% damaged cells (these cells are round, without intracellular granulation) wide cell lysis
4	Severe	100% damaged cells (these cells are round, without intracellular granulation) nearly complete destruction of the cell layers

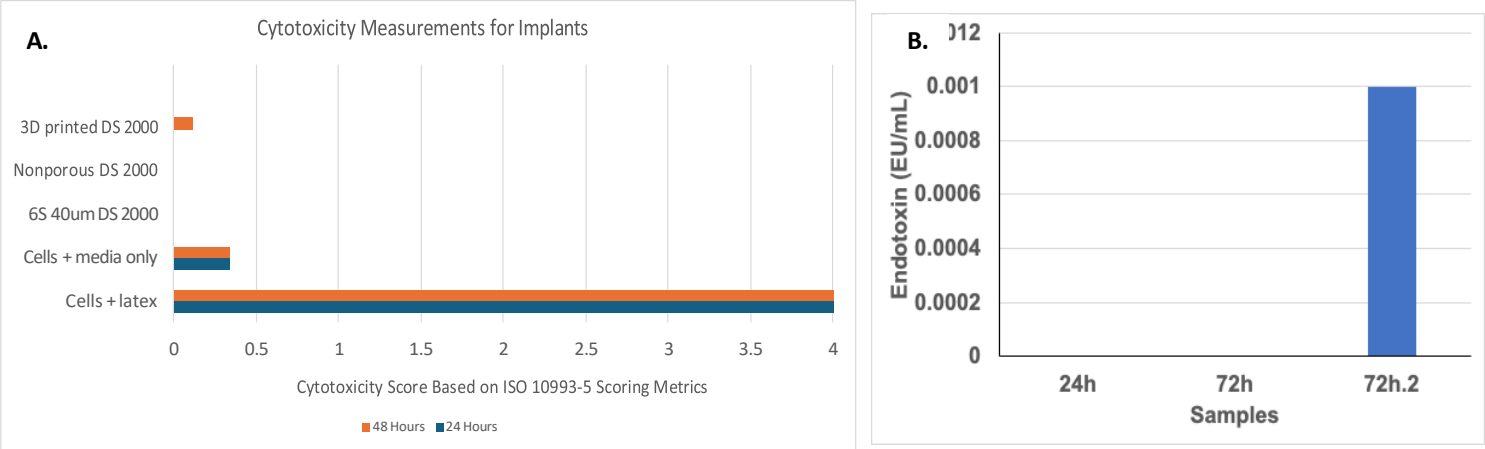

***Figure 20A:** Cytotoxicity testing results based on the guidelines provided in ISO: 10993-5. Materials are considered cytotoxic and fail the test if they receive a numerical grade greater than 2. Figure 20B: Endotoxicity results (post-blank) for 3D printed DS-2000 samples. The maximum concentration allowed to pass endotoxicity testing is .06 EU/mL*

3.8 Preliminary Histology results and discussions

Throughout the four-week animal implant study, all mice appeared to be in good health (Supplementary Figure 3), and no mice demonstrated signs of discomfort and/or pain. Following the explant procedure, all tissue samples were successfully harvested with the implant and nearby tissue site being intact in one piece. Unfortunately, during the subsequent embedding and sectioning process, multiple implants could not be properly located, and as such, some of the explanted tissue samples were damaged during the handling process. As a result, some of the sectioned tissue had large gaps of missing tissue near and surrounding the implant. Additionally, we experienced some of the implant "popping" out of the sectioned block, which resulted in a large circular void in the tissue where the implant should've been. In order to minimize variability, we elected to make all foreign body capsule measurements and cellularization measurements using only the remaining sectioned samples that contained both the implant and the surrounding tissue.

3.8.1 Fibrotic Capsule Thickness Measurements

We assessed the foreign body reaction to our 3D printed scaffolds by first measuring the thickness of the collagen capsule around our implant, which we quantified as the "fibrotic capsule". As shown in Figure 21A, there were two distinct sides for each sectioned sample; the left region with the thick blue area was the skin side, whereas the right region that contained the thick red area was the muscle side. However, underneath both the skin and the muscle regions, there was another thin, dense blue capsule that encapsulated all of the Porous Architectures in between the implant and the skin / muscle layers, which we believed was the collagen (fibrotic capsule) that formed due to the foreign body response. As shown in Figure 21B, this collagen layer was more densely packed, and the collagen fibers were stratified into parallel layers, which was in high contrast to the collagen from the natural skin, which was less densely packed and more random (wavy) in nature.

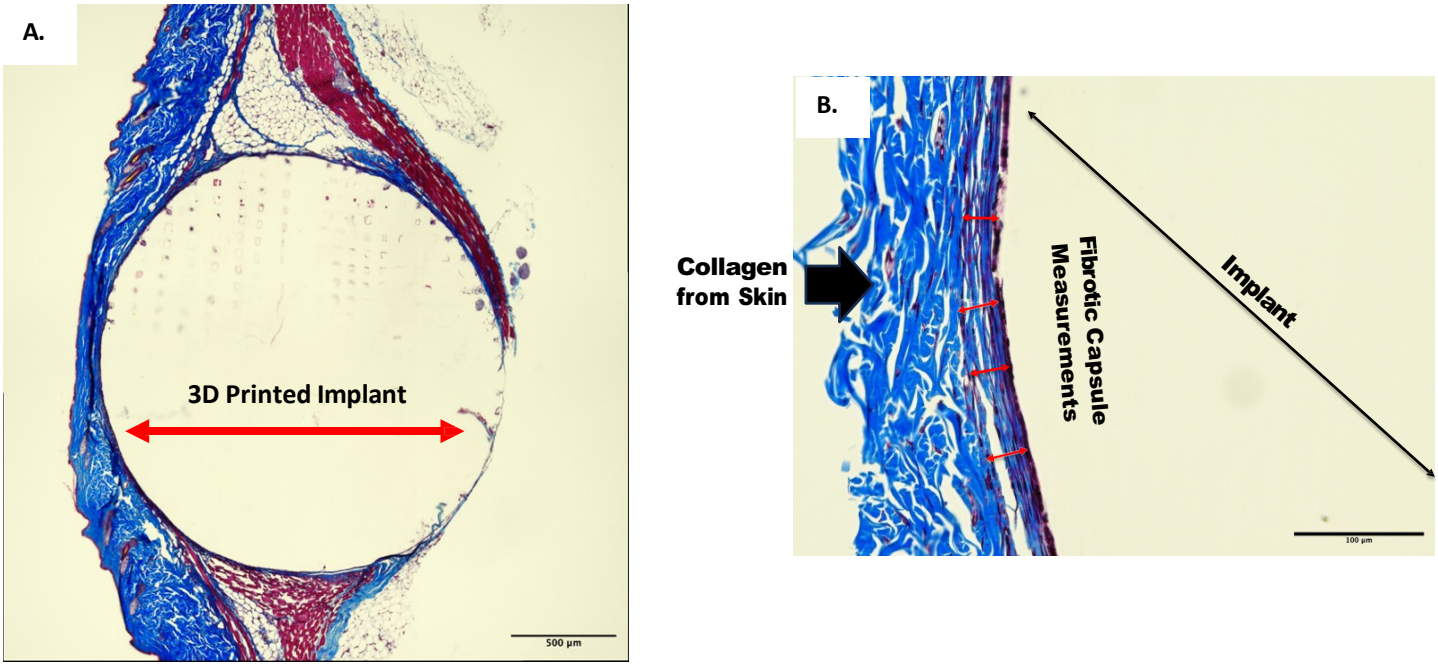

Figure 21A: *Mason's Trichrome stained cross-sections (Original Magnification 4x) of the implanted materials. A thin collagen capsule surrounded the implanted material across all Porous Architectures. Some tissue surrounding Porous Architecture C was unfortunately lost during the histology process.* ***Figure 21B:*** *High magnification (20x) image of the fibrotic capsule region around the implant. The fibrotic capsule layer has collagen that is stratified and more densely packed, whereas the natural collagen (identified by the thick black arrow) is more wavy and loosely packed. The fibrotic capsule thickness measurements were made by drawing a perpendicular line (as shown by the red arrows) from the edge of the implant interface to the approximate edge of the fibrotic capsule, and then measuring the length of that line using the scale bar.*

While all of the Porous Architectures in the 3D printed scaffolds displayed this collagen layer (Figure 22), we also noted that there was a similar response in all of the implanted control samples (Figure 23), which showed that even with the softer, pHEMA spherical shaped scaffolds containing 40 µm pores, it was difficult to fully mitigate the formation of a fibrotic capsule. We then quantified the average thicknesses of the fibrotic capsules around all of the implants by measuring the length of the perpendicular line drawn from the implant interface to the edge of the fibrotic capsule. The average thicknesses of the FBCs surrounding Porous Architecture A, B, C and D were 24.21 ± 3.45 µm, 29.09 ± 5.53 µm, 29.17 ± 5.29 µm and 36.54 ± 5.40 µm, whereas the average thicknesses of the fibrotic capsule for the pHEMA 40 µm, pHEMA 100 µm and the DS-2000 40 µm control samples were 19.84 ± 7.37 µm, 25.66 ± 9.78 µm, and 22.62 ± 3.52 µm, respectively.

In order to assess whether there was a statistical difference in the fibrotic capsule thicknesses, we used a one-way ANOVA test and Tukey's post-hoc (Figure 24), where we observed there was a statistical difference in the average fibrotic capsule thickness between Porous Architectures A, and B compared to Porous Architecture D measurements ($p = 0.0001$ and $p = 0.0213$, respectively), whereas there was no statistical difference for Porous Architecture C ($p = .0936$). Additionally, although there was no statistical difference in the average fibrotic capsule thickness for Porous Architecture A compared to both DS-2000 and pHEMA 40 µm scaffolds, both Porous Architecture C and D had statistically thicker fibrotic capsules compared to the pHEMA 40 µm scaffolds, although there was no statistical difference between Porous Architecture B and C against the DS-2000 controls (Figure 25)

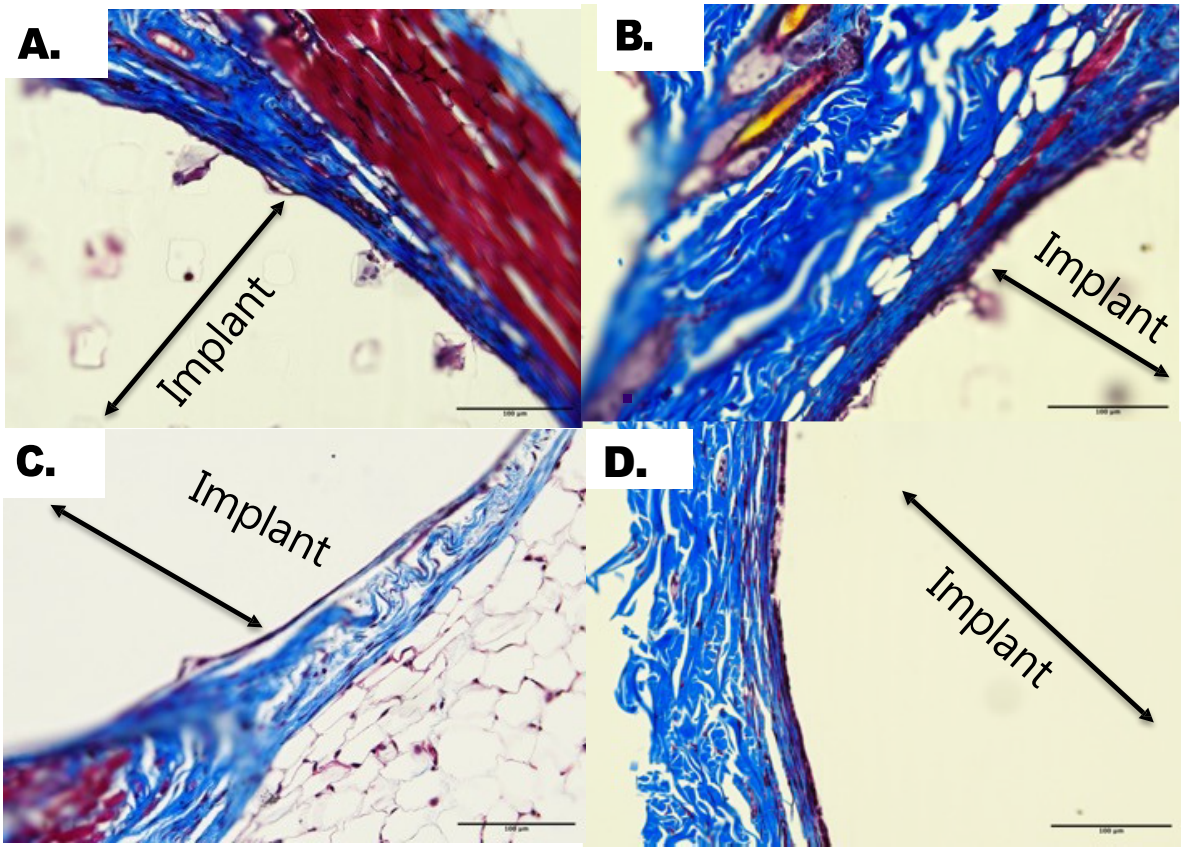

Figure 22: *High magnification (20x) image of the fibrotic capsule region around the 3D Printed Scaffolds. Image A shows Porous Architecture A, Image B shows Porous Architecture B, Image C shows Porous Architecture C, and Image D shows Porous Architecture D. Across all Porous Architectures, there is a clear fibrotic capsule formed, although the fibrotic capsule around Porous Architecture D appears to be thicker than the other areas. Unfortunately, the tissue surrounding Porous Architecture C was damaged during the embedding and sectioning process, and as a result, it was difficult to visualize the fibrotic capsule around this particular region.*

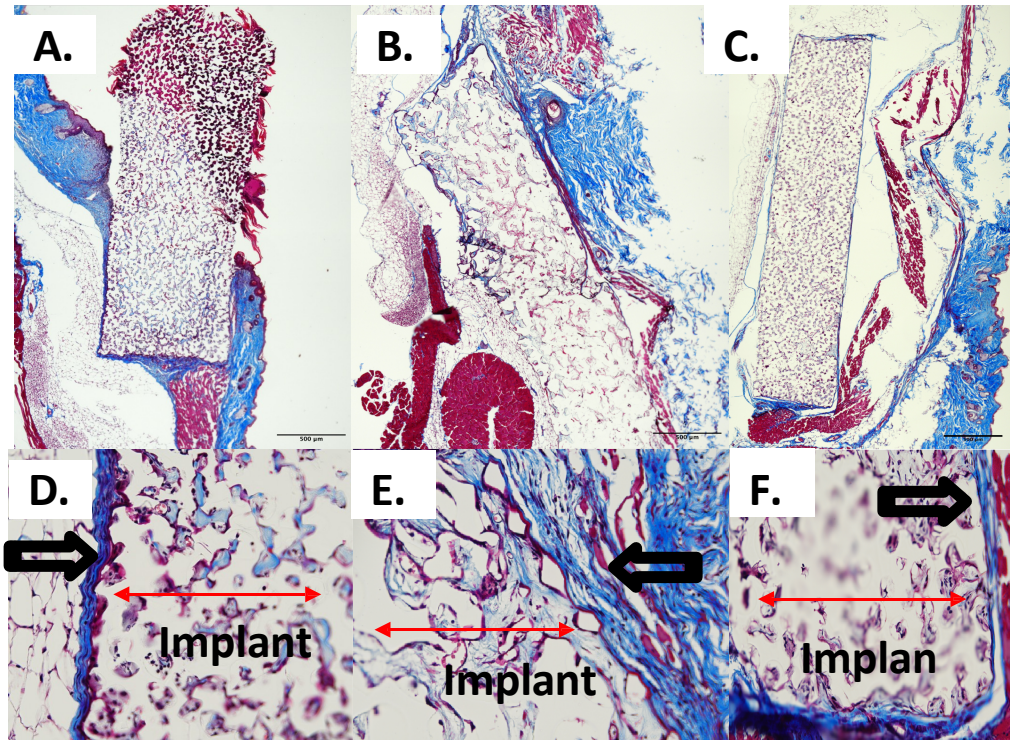

Figure 23: *Mason's Trichrome stained cross-sections of the implanted control (pHEMA 40 µm, pHEMA 100 µm and the DS-2000 40 µm) at 4x magnification (a), (b), and (c). A thin collagen capsule surrounded the implanted material, although pHEMA samples demonstrated smaller capsules compared to the DS-2000 samples.* ***Figure 23 D, E,F:*** *High magnification (x20) of the control samples, respectively. The collagen from the FBR is shown with the hollow black arrow.*

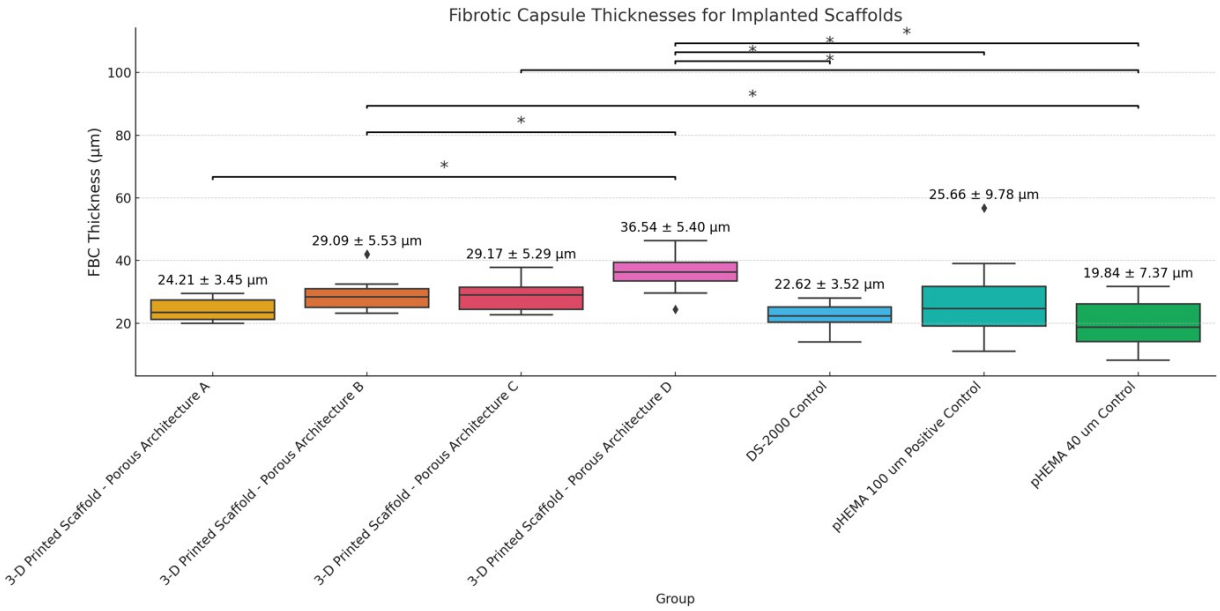

Figure 24: *Average fibrotic capsule thicknesses for each implanted scaffold. Average values were calculated from six random measurements made per each section, and for each explant, three sections were analyzed. Statistical significance is denoted by an *.*

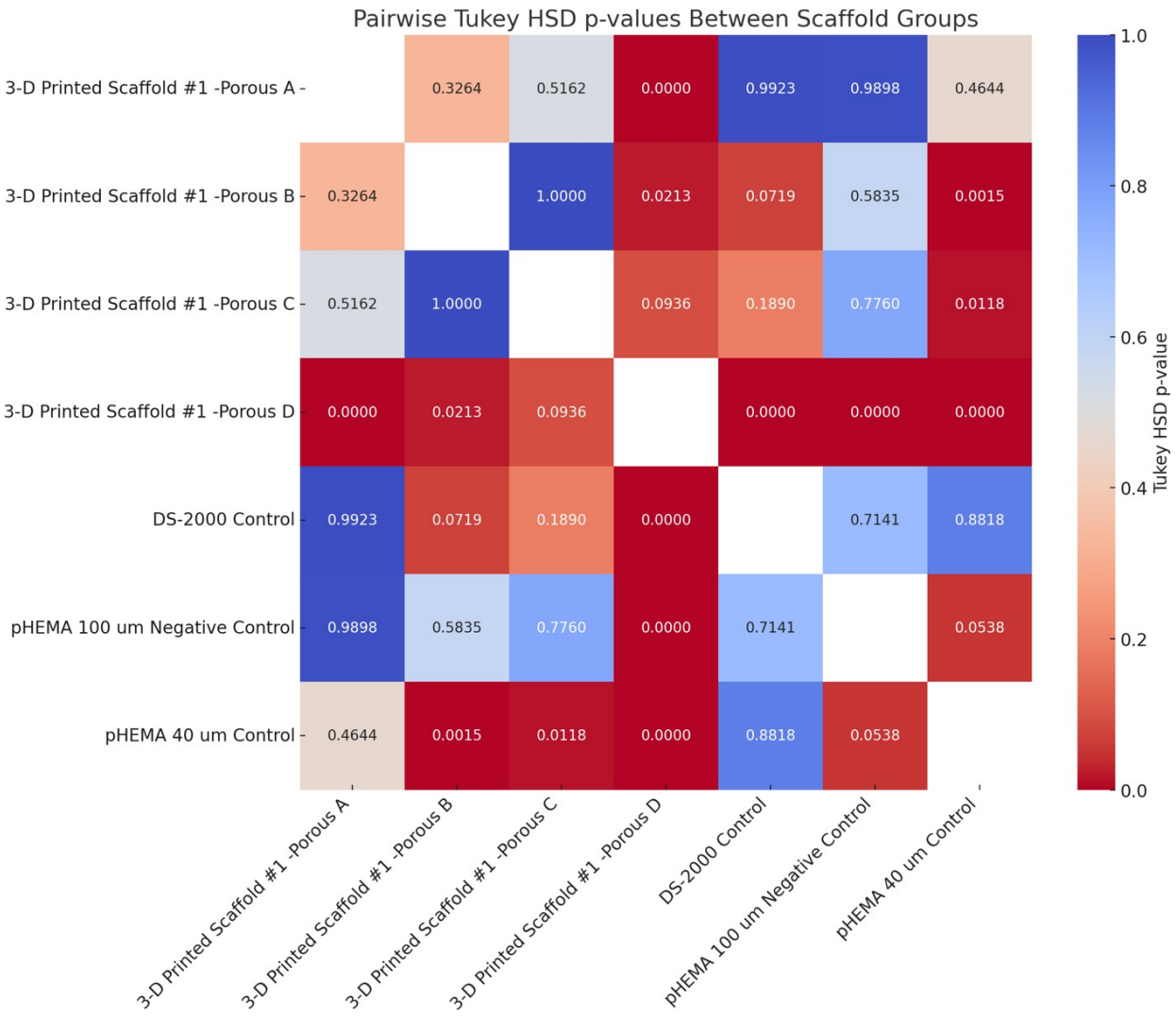

Figure 25: *Heatmap of the p-values following the one-way ANOVA and Tukey's post hoc testing. Statistical significance was determined when p < .05.*

Based on these results, we firstly concluded that while the control samples with the spherical 40 µm pores had on average thinner fibrotic capsules, it was possible to produce a similar fibrotic capsule response using the new porous scaffolds containing the 40 µm rectangular channels. Interestingly, as the rectangular channels were elongated, we observed that the mean fibrotic capsule thickness increased, which indicated that smaller channel sizes were favorable for reducing the overall fibrotic capsule thickness, which is aligned with the previous experimental results, where larger-pored pHEMA discs had thicker fibrotic capsules compared to the scaffolds with 40 µm pores[22].

However, despite the differences in the average values, there was no statistical difference in the mean fibrotic capsule thickness across Porous Architecture A, B and C, which could indicate that there might be a "threshold" in the immune activation, where once the scaffold reaches a certain degree of the foreign body response, the minor changes to the channel size doesn't amplify the thickness of the fibrotic capsule any further. Alternatively, these results could also be due to the effects of Porous Architecture A "bleeding" into the other

Porous Architectures via other cellular signals, etc. Unfortunately, we were unable to confirm this theory, but given the separation between each Porous Architecture is only 40 µm in the inner most regions, we theorize that it may have been possible for various pro-healing cytokines and other cellular factors from Porous Architecture A to influence the results in the other Porous Architectures. Additional immunohistochemistry data to assess for various pro-inflammatory and pro-healing cytokines may help better discern this theory.

Lastly, while these results suggest that porous scaffolds with 40 µm rectangular channels may have similar fibrotic capsule thicknesses to previously used scaffolds, further testing is required as we observed that the fibrotic capsule surrounding the pHEMA 100 µm scaffolds were not statistically different from both the DS-2000 samples and the pHEMA 40 µm samples, which is contrary to what was observed in other historical results around the same time point[22, 51]. While this could be due to the tissue being damaged during the embedding and sectioning process, which resulted in large gaps of missing tissue, further analysis is required to determine the role of the channel regions on the overall fibrotic capsule response.

3.8.2 Assessment for Cellularization Rate in Implanted Scaffolds

As the thickness of the fibrotic capsule is just one element of the foreign body response, we also elected to characterize the cellularization rates in each of the implanted scaffolds. As shown in Figure 26, we noticed that there was minimal cellularization in the 3D printed scaffolds, especially compared against both the 40 µm pHEMA and the 40 µm DS-2000 samples. As expected, after we analyzed our images to obtain an approximate cell density (Figure 27), there was a significant difference in the cell density values.

We hypothesize that the limited, and in some cases near-complete absence of, cellular infiltration into the porous scaffolds may be attributed to several factors. Firstly, we theorized that larger overall porous channel regions may also be unfavorable for cell infiltration, adhesion, similar to how the pHEMA 100 µm samples exhibited lower levels of cellularization. This is in good accordance with other historical experiments, where porous scaffolds with larger pores exhibited reduced polarization of macrophage cells towards the M2 state and vascularization[22, 51]. Additionally, other research indicates that the overall lower porosity experienced in the 3D printed structure (compared to the control samples) may have an adverse effect on the nutrient and waste exchange within these scaffolds, which further impacts the cell viability / proliferation rates[73]. Taken together, these results indicated that it may be necessary to have the smaller interconnects / smaller overall porous channels as well as increase the overall porosity of the structures in order to provide a better microenvironment for tissue integration, although additional work is needed to validate this theory.

However, it's also possible that the lower cellularization was due to partial occlusion of the internal pore architecture, particularly toward the center of the scaffold. This is especially evidenced in Porous Architecture C, where there were no pore / channels outlines observed (Figure 21/22 and Figure 26). Although it's unclear what the driving factor was behind the inner regions of our scaffolds being non-porous, as briefly stated, we hypothesized much of the occlusion was due to the highly viscous DS-2000 resin (600 mPa – 800 mPa) being trapped in the porous pockets within our scaffolds, and then being subsequently polymerized due to secondary polymerization, etc. Although the extent of this overcuring varied across the different Porous Architectures (evidenced by the presence of the pores in Porous Architecture A and B, albeit at smaller dimensions), we believe that the general shrinkage and occlusion of these pores may have contributed partially to the overall results we observed, although it's difficult to estimate the extent of this effect, as we observed that these pores were still, on average, larger than the historically used 16 µm interconnecting regions, which enabled cellular infiltration, etc. As such, we also suspect that the lack of cellularization may be due to the boundary artifacts (Figure 19 & Supplementary Figure 4) previously aforementioned creating localized defects that subsequently acted as additional barriers that further prevented cellular infiltration, particularly on the outer layers of our scaffolds. In

order to minimize this possibility, we recommend sanding the outer layers of the implanted scaffold post-washing in future studies.

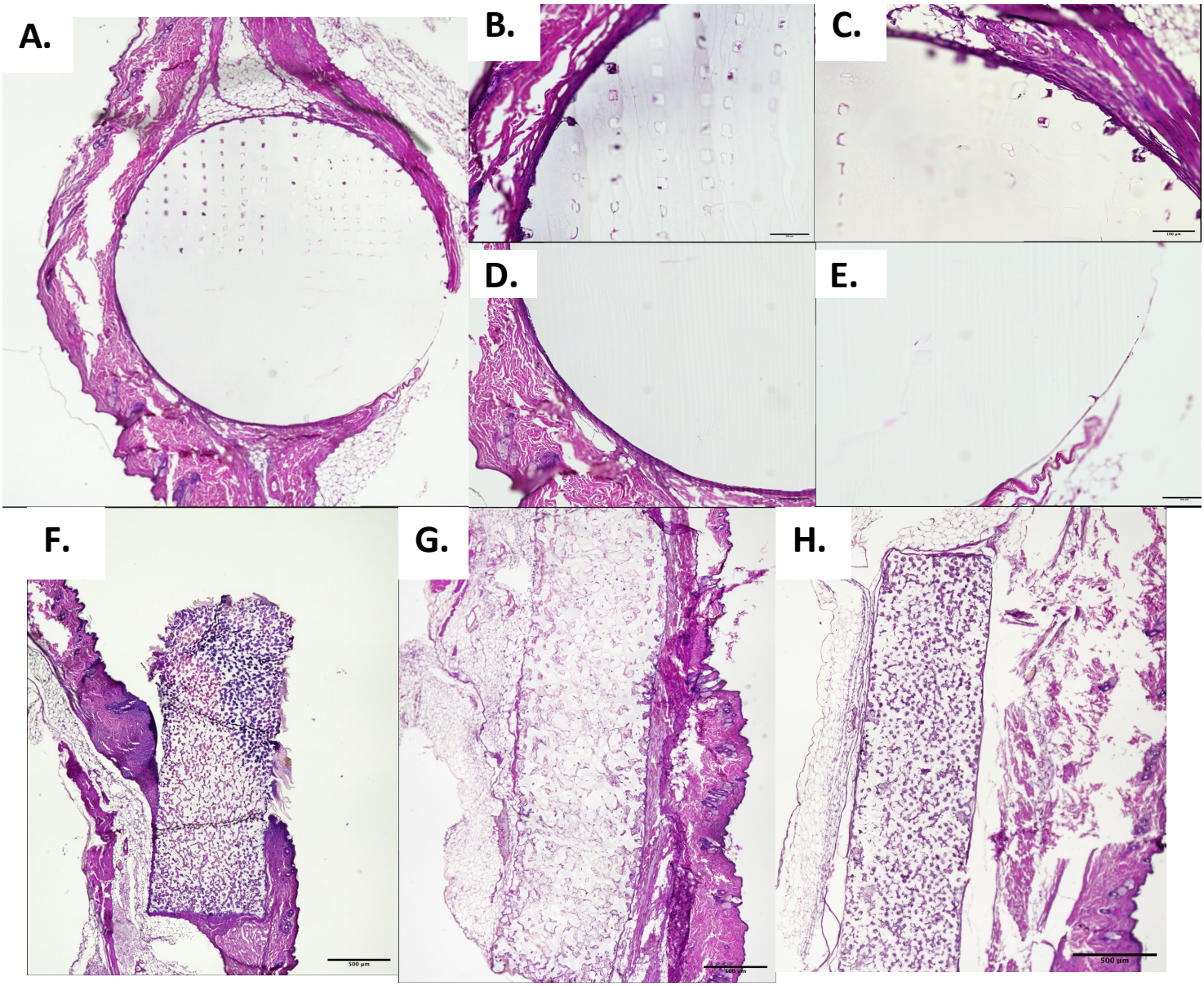

Figure 26: *H&E-stained cross-sections of the implanted materials (Original Magnification 4x and 20x). Representative high-powered images of each of the Porous Architectures are shown in Figure 26 B, C, D, and E. As shown in the high-powered images, there is a general lack of stained nuclei within the inner regions scaffolds, and on some occasions, the outlines of some pores were stained due to the serous fluid present in the pores.* ***Figure 26F, G, H:*** *Representative* H&E-stained cross-sections of the *pHEMA 40 µm, pHEMA 100 µm and DS-2000 40 µm samples, respectively*

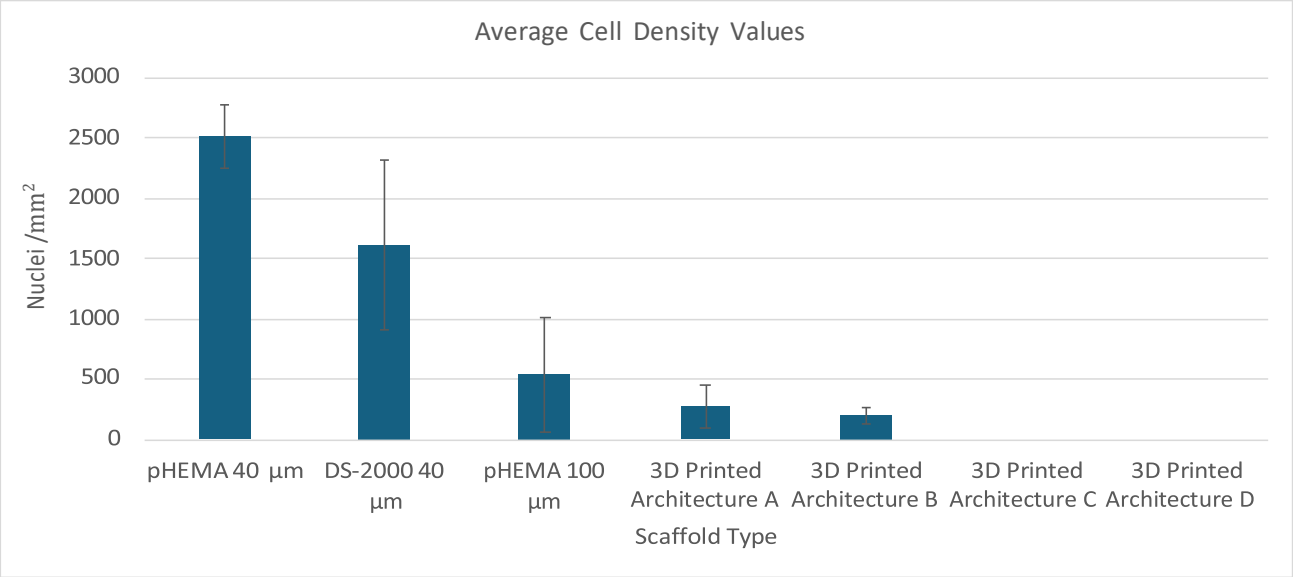

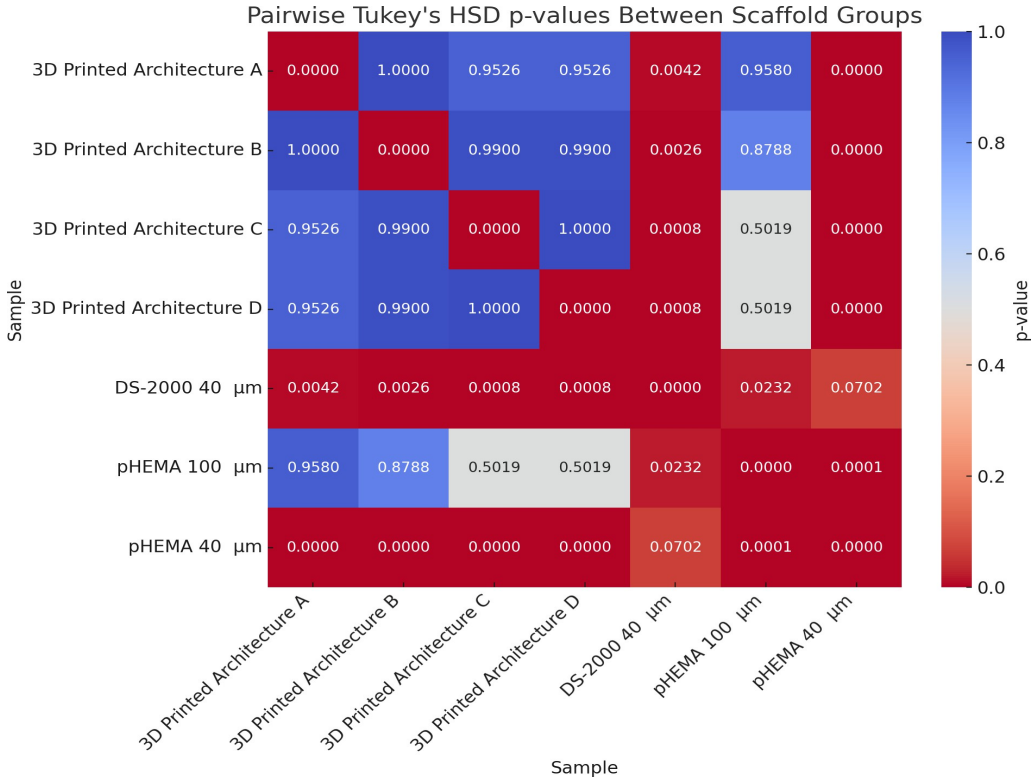

Figure 27 (top): *Cell density values, measured as nuclei / mm². The cell density measurements were based on an average of triplicate cell density calculations made from one section. Figure 27 (bottom): Heat map of all the generated p-values from the Tukey's post-hoc analysis. As shown, there was a statistical difference in the cell density when we compared the 3D printed scaffolds against both the pHEMA 40 µm and the DS-2000 40 µm samples, although there was no statistical difference observed between the cell density values calculated for the 3D printed scaffolds versus the pHEMA 100 µm samples.*

3.9 In Vitro Cellularization Results

In order to better understand the cellularization behavior, we opted to run one last in vitro experiment in hopes to understand whether the lack of cellularization was also observed in a more controlled environment.

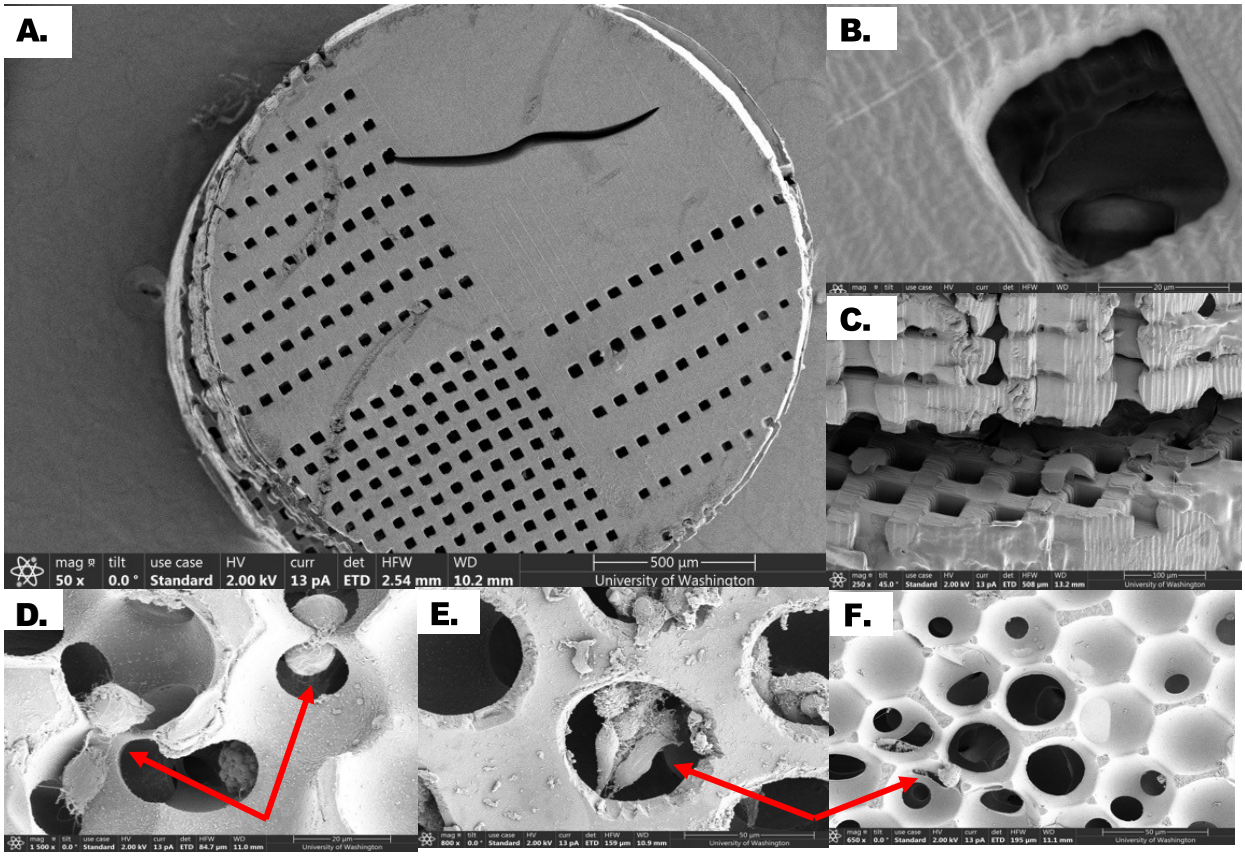

Figure 28: *SEM Images of the scaffolds post in vitro cellularization experiments. As shown in image A, B and C, there is no cell infiltration in the 3D printed scaffolds. However, in the pHEMA 40 µm (Image D), pHEMA 100 µm (Image E), and DS-2000 40 µm (Image F) scaffolds, there were cells infiltrating into the scaffolds, although the DS-2000 scaffolds had considerably less infiltration compared to the pHEMA samples*

As shown in Figure 28, there was no cell adhesion observed on the top layer of 3D printed scaffolds across any of the Porous Architectures. Furthermore, we observed no cell infiltration through the pores (Figure 28B), nor through any of the subsequent cross-sectional layers either (Image 28C). Conversely, all of the control samples demonstrated some cell infiltration and adhesion, which confirmed that the lack of cell infiltration was related to one of the variables associated with the 3D printed structures. Interestingly, while the DS-2000 40 µm samples did have some cellular infiltration, we visually observed that there were less cells infiltrating into the pores and adhering to the materials compared to the pHEMA samples, despite the same geometry / pore interconnectivity. This led us to conclude that while pore geometry does impact the degree of cellularization / integration, there are other factors, like the stiffness of DS-2000, that also impacted the overall ability of these scaffolds to enable cellular infiltration / cellularization. As such, while it's clear that the rectangular channels are unfavorable for cellular infiltration, future work should probe how the degree of cellularization would change if these porous scaffolds containing rectangular channels were made out of different materials, such as pHEMA.

CHAPTER 4: CONCLUSIONS

In this study, we successfully printed a porous scaffold containing multiple different porous architectures using a laser modulation value of 35%, and a laser velocity value of 60 mm/s. The resulting scaffold contained pores on the outer surfaces that were within the desired 30 – 40 µm range, as well as channel regions that were slightly below the target values (40 µm, 80 µm, 120 µm). Although there was a statistical difference in the pore size across the different porous architectures, where the pores in Porous Architecture A were smaller than the pores in Porous Architecture B and C, these observations were likely due to both the volume shrinkage and improper resin drainage problems. Following the *in vivo* experiments, we observed that Porous Architecture A had fibrotic capsule thicknesses similar to both the pHEMA 40 µm and DS-2000 controls samples, which indicated that it may be possible to use scaffolds with 40 µm rectangular channels instead of spherical pores with smaller interconnecting regions to elicit a similar response for fibrotic capsule thickness formation. However, when we assessed the cellularization capabilities of the 3-D printed scaffolds, we observed a significant difference in the cell density, where the 3D printed scaffolds across all Porous Architectures had significantly lower cell density counts. Although these results were likely attributed to a combination of unfavorable larger porous regions, coupled with the potential occlusion of the inner layer of the scaffold from improper resin drainage, and/or are a result of boundary artifacts forming localized defects that prevented cellular infiltration, these results indicated collectively that these 3D printed porous scaffolds with rectangular channels may be unfavorable for mitigating the overall foreign body reaction. However, while the immediate results from this research represents contrasting results from our original hypothesis, we showcased here the capability of using multi-design scaffolds to enable concurrent *in vivo* testing, and while additional modifications are required to better optimize these scaffolds, we believe that the ability to extract information of multiple designs from one device showcased the vast potential of these new multi-channel porous scaffolds for future research.

CHAPTER 5: FUTURE WORKS

Although we obtained preliminary data on the foreign body response to the fabricated scaffolds, additional work is still in progress, and a few of the key next steps are listed below.

In the short term, we propose using immunohistochemistry to better assess the behavior surrounding our implants. For instance, it would be interesting to assess the macrophage population surrounding each Porous Architecture, and identify, for example, whether there is a gradient of M2 markers as we move further away from the Porous Architecture A regions. Additionally, we would like to identify new methods to better slice the 3D printed scaffolds cross-sectionally to visualize the inner pore structures. We propose soaking the scaffolds in various solvents to soften the scaffolds, and/or re-design the scaffolds to be wider in order to better distributing the force during the slicing process.

Similarly, we would like to run additional volume shrinkage studies, in order to quantify the shrinkage rates for each scaffold region, and then use this information to pre-compensate for resin shrinkage by scaling the CAD models based on the observed shrinkage ratios. Likewise, it would also be interesting to assess whether different solvents with lower surface tension (such as hexanes) and/or other drying processes (such as critical point drying) can also better minimize the volume shrinkage issues, although these processes would be more costly than the current protocol. Additionally, it would also be interesting to test whether changing the printing orientation to print horizontally could better mitigate some of the resin drainage issues, since the distance the resin would need to travel out of the scaffold in the Z-direction would drastically be reduced and moreover, the amount of time between when each layer is fabricated should also be increased. Alternatively, we also propose experimenting

with other less viscous resins, such as the HEA blend produced by the Folch group, which we believe may also help minimize some of the overcuring issues we experienced in this research.

Finally, we propose running a new experiment to assess whether porous scaffolds with rectangular channels with a narrower channel regions (16 -20 µm W) can elicit a different overall response towards mitigating the FBR. This requires additional optimization of the printing settings in order to overcome the current obstacles in place towards fabricating porous structures with our 3D printer, but it would be interesting to observe whether the re-introduction of a narrower channel regions, across different lengths as well, can elicit a similar fibrotic capsule thickness to the control samples. Through this research, we hope to continue to advance our understanding of the role pore geometry, interconnecting regions, and channel size has on the foreign body response, in hopes to be able to create the next generation of engineered biomaterials with superior healing capabilities.

CHAPTER 6: REFERENCES

1. Bandyopadhyay, A.; Mitra, I.; Goodman, S. B.; Kumar, M.; Bose, S., Improving biocompatibility for next generation of metallic implants. *Progress in Materials Science* **2023,** *133*, 101053.
2. Prasad, K.; Bazaka, O.; Chua, M.; Rochford, M.; Fedrick, L.; Spoor, J.; Symes, R.; Tieppo, M.; Collins, C.; Cao, A.; Markwell, D.; Ostrikov, K. K.; Bazaka, K., Metallic Biomaterials: Current Challenges and Opportunities. *Materials (Basel)* **2017,** *10* (8).
3. Hauser, J.; Ring, A.; Schaffran, A.; Henrich, L.; Esenwein, S. A.; Steinau, H. U.; Stricker, I.; Langer, S., In vivo Analysis of Tissue Response to Plasma-Treated Collagen-I-Coated Titanium Alloys. *European Surgical Research* **2009,** *43* (3), 262-268.
4. Sorg, H.; Tilkorn, D. J.; Hauser, J.; Ring, A., Improving Vascularization of Biomaterials for Skin and Bone Regeneration by Surface Modification: A Narrative Review on Experimental Research. *Bioengineering (Basel)* **2022,** *9* (7).
5. Bose, S.; Robertson, S. F.; Bandyopadhyay, A., Surface modification of biomaterials and biomedical devices using additive manufacturing. *Acta Biomater* **2018,** *66*, 6-22.
6. Lee, S.-H.; Yoo, S.; Kim, S. H.; Kim, Y.-M.; Han, S. I.; Lee, H., Nature-inspired surface modification strategies for implantable devices. *Materials Today Bio* **2025,** *31*, 101615.
7. Jung, Y. H.; Kim, J. U.; Lee, J. S.; Shin, J. H.; Jung, W.; Ok, J.; Kim, T. I., Injectable Biomedical Devices for Sensing and Stimulating Internal Body Organs. *Adv Mater* **2020,** *32* (16), e1907478.
8. Zhang, D.; Chen, Q.; Shi, C.; Chen, M.; Ma, K.; Wan, J.; Liu, R., Dealing with the Foreign-Body Response to Implanted Biomaterials: Strategies and Applications of New Materials. *Advanced Functional Materials* **2021,** *31* (6), 2007226.
9. Albrektsson, T.; Wennerberg, A., On osseointegration in relation to implant surfaces. *Clin Implant Dent Relat Res* **2019,** *21 Suppl 1*, 4-7.
10. Ratner, B. D., Biomaterials: Been There, Done That, and Evolving into the Future. *Annual Review of Biomedical Engineering* **2019,** *21* (Volume 21, 2019), 171-191.
11. Anderson, J. M.; Rodriguez, A.; Chang, D. T., Foreign body reaction to biomaterials. *Semin Immunol* **2008,** *20* (2), 86-100.
12. Carnicer-Lombarte, A.; Chen, S.-T.; Malliaras, G. G.; Barone, D. G., Foreign Body Reaction to Implanted Biomaterials and Its Impact in Nerve Neuroprosthetics. *Frontiers in Bioengineering and Biotechnology* **2021,** *Volume 9 - 2021*.
13. Martin, K. E.; García, A. J., Macrophage phenotypes in tissue repair and the foreign body response: Implications for biomaterial-based regenerative medicine strategies. *Acta Biomater* **2021,** *133*, 4-16.
14. Franz, S.; Rammelt, S.; Scharnweber, D.; Simon, J. C., Immune responses to implants – A review of the implications for the design of immunomodulatory biomaterials. *Biomaterials* **2011,** *32* (28), 6692-6709.
15. Jones, J. A.; Chang, D. T.; Meyerson, H.; Colton, E.; Kwon, I. K.; Matsuda, T.; Anderson, J. M., Proteomic analysis and quantification of cytokines and chemokines from biomaterial surface-adherent macrophages and foreign body giant cells. *J Biomed Mater Res A* **2007,** *83* (3), 585-96.
16. Capuani, S.; Malgir, G.; Chua, C. Y. X.; Grattoni, A., Advanced strategies to thwart foreign body response to implantable devices. *Bioeng Transl Med* **2022,** *7* (3), e10300.
17. Tan, R. P.; Hallahan, N.; Kosobrodova, E.; Michael, P. L.; Wei, F.; Santos, M.; Lam, Y. T.; Chan, A. H. P.; Xiao, Y.; Bilek, M. M. M.; Thorn, P.; Wise, S. G., Bioactivation of Encapsulation Membranes Reduces Fibrosis and Enhances Cell Survival. *ACS Applied Materials & Interfaces* **2020,** *12* (51), 56908-56923.
18. Barr, S.; Hill, E. W.; Bayat, A., Development, fabrication and evaluation of a novel biomimetic human breast tissue derived breast implant surface. *Acta Biomaterialia* **2017,** *49*, 260-271.
19. Welch, N. G.; Winkler, D. A.; Thissen, H., Antifibrotic strategies for medical devices. *Advanced Drug Delivery Reviews* **2020,** *167*, 109-120.
20. Avula, M. N.; Rao, A. N.; McGill, L. D.; Grainger, D. W.; Solzbacher, F., Modulation of the foreign body response to implanted sensor models through device-based delivery of the tyrosine kinase inhibitor, masitinib. *Biomaterials* **2013,** *34* (38), 9737-9746.
21. Hernandez, J. L.; Woodrow, K. A., Medical Applications of Porous Biomaterials: Features of Porosity and Tissue-Specific Implications for Biocompatibility. *Advanced Healthcare Materials* **2022,** *11* (9), 2102087.

22. Sussman, E. M.; Halpin, M. C.; Muster, J.; Moon, R. T.; Ratner, B. D., Porous Implants Modulate Healing and Induce Shifts in Local Macrophage Polarization in the Foreign Body Reaction. *Annals of Biomedical Engineering* **2014,** *42* (7), 1508-1516.
23. Hady, T. F.; Hwang, B.; Waworuntu, R. L.; Ratner, B. D.; Bryers, J. D., Cells resident to precision templated 40-µm pore scaffolds generate small extracellular vesicles that affect CD4+ T cell phenotypes through regulatory TLR4 signaling. *Acta Biomaterialia* **2023,** *166*, 119-132.
24. Chan, N. R.; Hwang, B.; Ratner, B. D.; Bryers, J. D., Monocytes contribute to a pro-healing response in 40 µm diameter uniform-pore, precision-templated scaffolds. *Journal of Tissue Engineering and Regenerative Medicine* **2022,** *16* (3), 297-310.
25. Hady, T. F.; Hwang, B.; Pusic, A. D.; Waworuntu, R. L.; Mulligan, M.; Ratner, B.; Bryers, J. D., Uniform 40-µm-pore diameter precision templated scaffolds promote a pro-healing host response by extracellular vesicle immune communication. *J Tissue Eng Regen Med* **2021,** *15* (1), 24-36.
26. Chen, G.; Ratner, B. D., Vat Photopolymerization of Porous Scaffolds: Stabilization and Layer Thickness Control for Micron-Scale Accuracy. bioRxiv: 2025.
27. Veiseh, O.; Doloff, J. C.; Ma, M.; Vegas, A. J.; Tam, H. H.; Bader, A. R.; Li, J.; Langan, E.; Wyckoff, J.; Loo, W. S.; Jhunjhunwala, S.; Chiu, A.; Siebert, S.; Tang, K.; Hollister-Lock, J.; Aresta-Dasilva, S.; Bochenek, M.; Mendoza-Elias, J.; Wang, Y.; Qi, M.; Lavin, D. M.; Chen, M.; Dholakia, N.; Thakrar, R.; Lacík, I.; Weir, G. C.; Oberholzer, J.; Greiner, D. L.; Langer, R.; Anderson, D. G., Size- and shape-dependent foreign body immune response to materials implanted in rodents and non-human primates. *Nat Mater* **2015,** *14* (6), 643-51.
28. Paul, K.; Darzi, S.; O'Connell, C. D.; Hennes, D.; Rosamilia, A.; Gargett, C. E.; Werkmeister, J. A.; Mukherjee, S., *3D Printed Mesh Geometry Modulates Immune Response and Interface Biology in Mouse and Sheep Model: Implications for Pelvic Floor Surgery (Adv. Sci. 11/2025)*. Adv Sci (Weinh). 2025 Mar 20;12(11):2570075. doi: 10.1002/advs.202570075. eCollection 2025 Mar.
29. Mukasheva, F.; Adilova, L.; Dyussenbinov, A.; Yernaimanova, B.; Abilev, M.; Akilbekova, D., Optimizing scaffold pore size for tissue engineering: insights across various tissue types. *Frontiers in Bioengineering and Biotechnology* **2024,** *Volume 12 - 2024*.
30. Jordan, S. W.; Fligor, J. E.; Janes, L. E.; Dumanian, G. A., Implant Porosity and the Foreign Body Response. *Plast Reconstr Surg* **2018,** *141* (1), 103e-112e.
31. Zhou, X.; Wang, Y.; Ji, J.; Zhang, P., Materials Strategies to Overcome the Foreign Body Response. *Adv Healthc Mater* **2024,** *13* (18), e2304478.
32. Kyriakides, T. R.; Kim, H. J.; Zheng, C.; Harkins, L.; Tao, W.; Deschenes, E., Foreign body response to synthetic polymer biomaterials and the role of adaptive immunity. *Biomed Mater* **2022,** *17* (2).
33. Cheng, A.; Schwartz, Z.; Kahn, A.; Li, X.; Shao, Z.; Sun, M.; Ao, Y.; Boyan, B. D.; Chen, H., Advances in Porous Scaffold Design for Bone and Cartilage Tissue Engineering and Regeneration. *Tissue Engineering Part B: Reviews* **2018,** *25* (1), 14-29.
34. Li, W.; Dai, F.; Zhang, S.; Xu, F.; Xu, Z.; Liao, S.; Zeng, L.; Song, L.; Ai, F., Pore Size of 3D-Printed Polycaprolactone/Polyethylene Glycol/Hydroxyapatite Scaffolds Affects Bone Regeneration by Modulating Macrophage Polarization and the Foreign Body Response. *ACS Applied Materials & Interfaces* **2022,** *14* (18), 20693-20707.
35. Chan, N. R.; Hwang, B.; Mulligan, M. S.; Ratner, B. D.; Bryers, J. D., Porous Precision-Templated 40 µm Pore Scaffolds Promote Healing through Synergy in Macrophage Receptor with Collagenous Structure and Toll-Like Receptor Signaling. *Tissue Eng Part A* **2024,** *30* (7-8), 287-298.
36. Kim, H. J.; Kim, U.-J.; Vunjak-Novakovic, G.; Min, B.-H.; Kaplan, D. L., Influence of macroporous protein scaffolds on bone tissue engineering from bone marrow stem cells. *Biomaterials* **2005,** *26* (21), 4442-4452.
37. Li, W. L.; Lu, K.; Walz, J. Y., Freeze casting of porous materials: review of critical factors in microstructure evolution. *International Materials Reviews* **2012,** *57* (1), 37-60.
38. Kang, H.-W.; Tabata, Y.; Ikada, Y., Fabrication of porous gelatin scaffolds for tissue engineering. *Biomaterials* **1999,** *20* (14), 1339-1344.
39. Accardo, A.; Courson, R.; Riesco, R.; Raimbault, V.; Malaquin, L., Direct laser fabrication of meso-scale 2D and 3D architectures with micrometric feature resolution. *Additive Manufacturing* **2018,** *22*, 440-446.
40. Vaquette, C.; Cooper-White, J. J., Increasing electrospun scaffold pore size with tailored collectors for improved cell penetration. *Acta Biomaterialia* **2011,** *7* (6), 2544-2557.

41. Leong, M. F.; Rasheed, M. Z.; Lim, T. C.; Chian, K. S., In vitro cell infiltration and in vivo cell infiltration and vascularization in a fibrous, highly porous poly(D,L-lactide) scaffold fabricated by cryogenic electrospinning technique. *Journal of Biomedical Materials Research Part A* **2009,** *91A* (1), 231-240.
42. Annabi, N.; Mithieux, S. M.; Weiss, A. S.; Dehghani, F., The fabrication of elastin-based hydrogels using high pressure CO2. *Biomaterials* **2009,** *30* (1), 1-7.
43. Zhen, L.; Creason, S. A.; Simonovsky, F. I.; Snyder, J. M.; Lindhartsen, S. L.; Mecwan, M. M.; Johnson, B. W.; Himmelfarb, J.; Ratner, B. D., Precision-porous polyurethane elastomers engineered for application in pro-healing vascular grafts: Synthesis, fabrication and detailed biocompatibility assessment. *Biomaterials* **2021,** *279*, 121174.
44. Madden, L. R.; Mortisen, D. J.; Sussman, E. M.; Dupras, S. K.; Fugate, J. A.; Cuy, J. L.; Hauch, K. D.; Laflamme, M. A.; Murry, C. E.; Ratner, B. D., Proangiogenic scaffolds as functional templates for cardiac tissue engineering. *Proceedings of the National Academy of Sciences* **2010,** *107* (34), 15211-15216.
45. Kim, S. Y.; Nair, M. G., Macrophages in wound healing: activation and plasticity. *Immunol Cell Biol* **2019,** *97* (3), 258-267.
46. McWhorter, F. Y.; Wang, T.; Nguyen, P.; Chung, T.; Liu, W. F., Modulation of macrophage phenotype by cell shape. *Proceedings of the National Academy of Sciences* **2013,** *110* (43), 17253-17258.
47. Tylek, T.; Blum, C.; Hrynevich, A.; Schlegelmilch, K.; Schilling, T.; Dalton, P. D.; Groll, J., Precisely defined fiber scaffolds with 40 µm porosity induce elongation driven M2-like polarization of human macrophages. *Biofabrication* **2020,** *12* (2), 025007.
48. Liu, Y.; Suarez-Arnedo, A.; Riley, L.; Miley, T.; Xia, J.; Segura, T., Spatial confinement modulates macrophage response in microporous annealed particle (MAP) scaffolds. bioRxiv: 2023.
49. Zhen, L.; Quiroga, E.; Creason, S. A.; Chen, N.; Sapre, T. R.; Snyder, J. M.; Lindhartsen, S. L.; Fountaine, B. S.; Barbour, M. C.; Faisal, S.; Aliseda, A.; Johnson, B. W.; Himmelfarb, J.; Ratner, B. D., Synthetic vascular graft that heals and regenerates. *Biomaterials* **2025,** *320*, 123206.
50. Wyatt, M. Precision-Porous Biomaterials for Skin Healing. ProQuest Dissertations & Theses, 2024.
51. Guoyao Chen, S. C., Ningjing Chen, Adia Kirkham, Le Zhen, Shijie Zhang. Kan Wu, Buddy Ratner 3D-Printed Precision Porous Scaffolds Promote Healing In Vivo [Manuscript submitted for publication]. *For consideration in Journal of Biomedical Materials Research* **2025**, 21.
52. Chen, G.; Ratner, B. D. A high-resolution 3D printable porous biomaterial. [University of Washington Libraries], Seattle, 2020.
53. Muallah, D.; Sembdner, P.; Holtzhausen, S.; Meissner, H.; Hutsky, A.; Ellmann, D.; Assmann, A.; Schulz, M. C.; Lauer, G.; Kroschwald, L. M., Adapting the Pore Size of Individual, 3D-Printed CPC Scaffolds in Maxillofacial Surgery. *Journal of Clinical Medicine* **2021,** *10* (12), 2654.
54. Liu, T.; Wang, Y.; Kuang, T., Oriented Porous Polymer Scaffolds in Tissue Engineering: A Comprehensive Review of Preparation Strategies and Applications. *Macromolecular Materials and Engineering* **2024,** *309* (1), 2300246.
55. Abbasi, N.; Hamlet, S.; Love, R. M.; Nguyen, N.-T., Porous scaffolds for bone regeneration. *Journal of Science: Advanced Materials and Devices* **2020,** *5* (1), 1-9.
56. Kang, Y.; and Chang, J., Channels in a Porous Scaffold: a New Player for Vascularization. *Regenerative Medicine* **2018,** *13* (6), 705-715.
57. Prem Ananth, K.; Jayram, N. D., A comprehensive review of 3D printing techniques for biomaterial-based scaffold fabrication in bone tissue engineering. *Annals of 3D Printed Medicine* **2024,** *13*, 100141.
58. Gao, Y.; Lalevée, J.; Simon‐Masseron, A., An Overview on 3D Printing of Structured Porous Materials and Their Applications. *Advanced Materials Technologies* **2023,** *8* (17).
59. <US4575330.pdf>.
60. Batch, G. L.; Macosko, C. W., Oxygen inhibition in differential scanning calorimetry of free radical polymerization. *Thermochimica Acta* **1990,** *166*, 185-198.
61. He, H.; Pan, Y.; Feinerman, A.; Xu, J., Air-Diffusion-Channel Constrained Surface Based Stereolithography for Three-Dimensional Printing of Objects With Wide Solid Cross Sections. *Journal of Manufacturing Science and Engineering* **2018,** *140* (6).

62. Melchels, F. P. W.; Feijen, J.; Grijpma, D. W., A review on stereolithography and its applications in biomedical engineering. *Biomaterials* **2010,** *31* (24), 6121-6130.
63. Topa-Skwarczyńska, M.; Ortyl, J., Photopolymerization shrinkage: strategies for reduction, measurement methods and future insights. *Polymer Chemistry* **2023,** *14* (18), 2145-2158.
64. Zhang, Q.; Weng, S.; Hamel, C. M.; Montgomery, S. M.; Wu, J.; Kuang, X.; Zhou, K.; Qi, H. J., Design for the reduction of volume shrinkage-induced distortion in digital light processing 3D printing. *Extreme Mechanics Letters* **2021,** *48*, 101403.
65. Fair, E.; Bornstein, J.; Lyons, T.; Sgobba, P.; Hayes, A.; Rourke, M.; Macwan, I.; Haghbin, N., Evaluating the efficacy of uniformly designed square mesh resin 3D printed scaffolds in directing the orientation of electrospun PCL nanofibers. *Scientific Reports* **2024,** *14* (1), 22722.
66. Park, J. Y.; Jung, Y. N.; Jang, K. J.; Lee, S. K.; Choi, S. W.; Lee, Y. S.; Yang, Y. P.; Yun, K. D., Effect of Axis Change on Shrinkage Rate of 3D-Printed Bioceramic Zirconia Fabricated via Digital Light Processing. *Biomimetics (Basel)* **2025,** *10* (3).
67. Arora, P.; Mostafa, K. G.; Russell, E.; Dehgahi, S.; Butt, S. U.; Talamona, D.; Qureshi, A. J., Shrinkage Compensation and Effect of Building Orientation on Mechanical Properties of Ceramic Stereolithography Parts. *Polymers* **2023,** *15* (19), 3877.
68. Mohanty, S.; Larsen, L. B.; Trifol, J.; Szabo, P.; Burri, H. V. R.; Canali, C.; Dufva, M.; Emnéus, J.; Wolff, A., Fabrication of scalable and structured tissue engineering scaffolds using water dissolvable sacrificial 3D printed moulds. *Materials Science and Engineering: C* **2015,** *55*, 569-578.
69. Ghosh, T.; Fritz, E.-C.; Balakrishnan, D.; Zhang, Z.; Vrancken, N.; Anand, U.; Zhang, H.; Loh, N. D.; Xu, X.; Holsteyns, F.; Nijhuis, C. A.; Mirsaidov, U., Preventing the Capillary-Induced Collapse of Vertical Nanostructures. *ACS Applied Materials & Interfaces* **2022,** *14* (4), 5537-5544.
70. Chini, S. F.; Amirfazli, A., Understanding Pattern Collapse in Photolithography Process Due to Capillary Forces. *Langmuir* **2010,** *26* (16), 13707-13714.
71. Liu, K.; Zhou, Q.; Zhang, X.; Ma, L.; Xu, B.; He, R., Morphologies, mechanical and in vitro behaviors of DLP-based 3D printed HA scaffolds with different structural configurations. *RSC Adv* **2023,** *13* (30), 20830-20838.
72. Denis, C.; Robberecht, L.; Delattre, J.; Deveaux, E.; Hornez, J.-C.; Dehurtevent, M., Effect of dimensional variations on the manufacturing process and the 3D shrinkage ratio of stereolithographic dental alumina ceramics. *Dental Materials Journal* **2023,** *42* (1), 79-85.
73. Ruiz-Cantu, L.; Gleadall, A.; Faris, C.; Segal, J.; Shakesheff, K.; Yang, J., Characterisation of the surface structure of 3D printed scaffolds for cell infiltration and surgical suturing. *Biofabrication* **2016,** *8* (1), 015016.

***Supplementary Table 1**: Analysis of Pore Size Measurements made in X versus Z Direction for Porous Architecture A*

LAYER #	X1	X2	X3	Z1	Z2	Z3	Mean (X-direction)	Mean (Z-direction)	T-statistic	P-value
Layer 1	26.672	32.2066667	36.3836667	34.3103333	37.1263333	27.5583333	31.75411111	32.99833333	-0.244176851	0.82985833
Layer 2										
Layer 3	29.7216667	35.0496667	38.9993333	32.9266667	32.5826667	24.7733333	34.59022222	30.09422222	0.875876078	0.473466976
Layer 4										
Layer 5	28.1256667	31.2726667	38.1533333	29.8873333	35.6393333	29.039	32.51722222	31.52188889	0.241084622	0.831951758
Layer 6										
Layer 7	30.639	32.3513333	35.077	34.9803333	32.471	30.8086667	32.68911111	32.75333333	-0.025838221	0.981732667
Layer 8										
Layer 9	30.7416667	32.5246667	36.231	32.97	35.2786667	31.7116667	33.16577778	33.32011111	-0.065904983	0.953448661
Layer 10										
Layer 11	33.445	33.9983333	33.2963333	32.7673333	31.2673333	30.982	33.57988889	31.67222222	3.04422072	0.093084973
Layer 12										
Layer 13	30.5386667	28.9256667	35.8316667	35.9203333	35.018	28.381	31.76533334	33.10644444	-0.304751338	0.789343849
Layer 14										
Layer 15	30.7676667	30.8933333	38.2723333	36.5276667	35.7363333	34.3106667	33.31111111	35.52488889	-0.714341084	0.549137339
Layer 16										
Layer 17	34.104	30.8806667	34.5933333	34.051	38.234	27.297	33.19266667	33.194	-0.000315277	0.999777065
Layer 18										
Layer 19	33.4586667	28.5533333	36.1996667	34.0003333	37.94	29.6206667	32.73722222	33.85366667	-0.24176755	0.831489221
Layer 20										
Layer 21	33.0093333	32.9796667	41.7063333	33.7413333	39.0676667	27.7263333	35.89844444	33.51177778	0.397822503	0.729207153
Layer 22										
Layer 23	31.1453333	33.922	42.5593333	34.2183333	37.2186667	31.348	35.87555555	34.26166667	0.336285941	0.768660445
Layer 24										
Layer 25	29.7856667	31.426	39.1306667	34.8063333	39.169	29.3356667	33.44744445	34.437	-0.181595044	0.872638612
Layer 26										
Layer 27	30.5343333	33.775	38.6963333	32.8993333	39.0213333	29.97	34.33522222	33.96355555	0.087259272	0.938415495
Layer 28										
Layer 29	28.9643333	33.358	36.7306667	37.8623333	38.977	29.104	33.01766667	35.31444444	-0.454698963	0.693911309
Layer 30										
Layer 31	30.5326667	32.5053333	35.8463333	34.1246667	37.3866667	28.1253333	32.96144444	33.21222222	-0.062643877	0.955747483
Layer 32										
Layer 33	30.9966667	34.416	28.1036667	33.0676667	37.2063333	23.9156667	31.17211111	31.39655556	-0.101284826	0.928563788
Layer 34										
Layer 35	34.1233333	32.5793333	32.058	35.156	37.7786667	23.428	32.92022222	32.12088889	0.195153354	0.86330114
Layer 36										
Layer 37	31.8213333	33.7086667	31.232	36.187	38.7076667	25.232	32.254	33.37555556	-0.314560517	0.782878247
Layer 38										
Layer 39	30.128	36.8006667	36.7466667	36.9966667	39.5583333	26.4356667	34.55844445	34.33022222	0.044065273	0.968856261
Layer 40										
Layer 41	34.116	32.2423333	34.0843333	35.845	37.2873333	24.9306667	33.48088889	32.68766667	0.184968242	0.870312258
Layer 42										
Layer 43	29.928	33.2616667	38.0736667	36.7976667	40.5406667	28.4336667	33.75444445	35.25733334	-0.269687871	0.812677526
Layer 44										
Layer 45	30.9883333	32.398	41.109	37.5216667	35.2313333	30.6503333	34.83177778	34.46777778	0.070554817	0.950172183
Layer 46										
Layer 47	32.1756667	36.5113333	39.7983333	38.112	33.8743333	30.155	36.16177778	34.04711111	0.469400309	0.684983025
Layer 48										
Layer 49	31.2093333	35.576	36.283	37.801	37.3203333	31.272	34.35611111	35.46444444	-0.329423514	0.773135915
Layer 50										
Layer 51	32.6	30.407	38.4706667	35.3896667	37.0936667	30.4003333	33.82588889	34.29455556	-0.10614794	0.92515261
Layer 52										
Layer 53	35.5023333	32.1479333	36.944	38.796	36.7696667	31.9963333	34.86475555	35.854	-0.330507195	0.772428206
Layer 54										
Layer 55	32.14	30.3846667	38.2483333	35.7266667	35.618	34.1646667	33.591	35.16977778	-0.549933955	0.637575484
Layer 56										
Layer 57	33.498	29.786	40.5186667	34.5713333	37.4166667	34.58	34.60088889	35.52266667	-0.235275712	0.835890505
Layer 58										
Layer 59	34.8143333	33.3393333	39.5803333	36.3326667	39.082	30.9073333	35.91133333	35.44066667	0.11000413	0.922449587
Layer 60										
Layer 61	31.8593333	29.8303333	43.2906667	34.9766667	36.767	31.0826667	34.99344444	34.27544445	0.122738389	0.913535882
Layer 62										
Layer 63	33.9543333	34.88	33.0956667	32.879	33.6236667	33.851	33.97666667	33.45122222	0.81779081	0.499405941
Layer 64										
Layer 65	34.8403333	35.08	35.8753333	35.5796667	38.782	33.911	35.26522222	36.09088889	-0.504594002	0.66394847
Layer 66										
Layer 67	34.8123333	32.0363333	40.431	35.4903333	42.13	34.52	35.75988889	37.38011111	-0.348877059	0.760487122
Layer 68										
Layer 69	36.858	36.3193333	38.802	32.117	32.135	36.07	37.32644444	33.44066667	6.488709372	0.022937069
Layer 70										

***Supplementary Table 2**: Analysis of Pore Size Measurements made in X versus Z Direction for Porous Architecture B*

LAYER #	X1	X2	X3	Z1	Z2	Z3	Mean (X-direction)	Mean (Z-direction)	T-statistic	P-value
Layer 1	35.125	31.2093333	35.154	30.511	30.5656667	33.195	33.82944444	31.42388889	2.06011141	0.175563506
Layer 2										
Layer 3										
Layer 4	31.6063333	35.8576667	32.777	27.544	32.537	33.616	33.41366667	31.23233333	1.43013118	0.288947218
Layer 5										
Layer 6										
Layer 7	34.7173333	34.6133333	33.899	33.2513333	32.9436667	31.8036667	34.40988889	32.66622222	9.40477036	0.011117669
Layer 8										
Layer 9										
Layer 10	35.2723333	34.798	35.7113333	36.4566667	35.1916667	35.2863333	35.26055555	35.64488889	-0.8272385	0.495090752
Layer 11										
Layer 12										
Layer 13	35.3863333	35.4383333	32.3606667	28.0336667	29.6786667	32.7903333	34.39511111	30.16755556	1.78108538	0.216851087
Layer 14										
Layer 15										
Layer 16	37.9206667	37.473	33.6176667	37.522	37.638	34.621	36.33711111	36.59366667	-0.6298883	0.59313406
Layer 17										
Layer 18										
Layer 19	38.446	33.81	34.4956667	31.068	36.5086667	31.3806667	35.58388889	32.98577778	0.88966003	0.467517113
Layer 20										
Layer 21										
Layer 22	33.83	37.127	34.4716667	34.3216667	33.7413333	32.797	35.14288889	33.62	1.35746853	0.307515026
Layer 23										
Layer 24										
Layer 25	37.033	35.0246667	35.5963333	32.062	37.2613333	31.5416667	35.88466667	33.62166667	0.99897123	0.423045907
Layer 26										
Layer 27										
Layer 28	35.3926667	34.7316667	35.6313333	31.2223333	40.8403333	32.1396667	35.25188889	34.73411111	0.15600371	0.890353823
Layer 29										
Layer 30										
Layer 31	38.1926667	33.7213333	37.9213333	33.4186667	34.0556667	33.3656667	36.61177778	33.61333334	1.79808089	0.213986654
Layer 32										
Layer 33										
Layer 34	37.9166667	39.1856667	38.191	31.9736667	33.4923333	35.8373333	38.43111111	33.76777778	4.03025955	0.056406411
Layer 35										
Layer 36										
Layer 37	36.1116667	35.0096667	37.7883333	31.5576667	34.7383333	31.271	36.30322222	32.52233333	2.05033373	0.176822923
Layer 38										
Layer 39										
Layer 40	36.9923333	40.2113333	38.112	31.6976667	35.1453333	31.2626667	38.43855555	32.70188889	10.239736	0.00940293
Layer 41										
Layer 42										
Layer 43	40.1023333	36.26	37.4526667	33.6006667	35.829	34.1973333	37.93833333	34.54233333	1.93629903	0.192455093
Layer 44										
Layer 45										
Layer 46	37.947	36.518	42.3923333	32.8873333	36.4093333	36.8243333	38.95244444	35.37366666	2.05529241	0.176182695
Layer 47										
Layer 48										
Layer 49	42.4293333	35.264	40.389	32.946	36.384	36.4816667	39.36077778	35.27055556	1.33567683	0.313368128
Layer 50										
Layer 51										
Layer 52	36.64	43.345	37.101	30.1173333	35.7273333	34.777	39.02866667	33.54055555	3.4017387	0.076617145
Layer 53										
Layer 54										
Layer 55	35.4903333	38.419	39.6226667	31.2436667	33.6276667	36.735	37.844	33.86877778	7.02270228	0.019679857
Layer 56										
Layer 57										
Layer 58	39.566	40.4305	38.3236667	31.0983333	27.372	39.3896667	39.44005556	32.62	1.63952262	0.242780104
Layer 59										
Layer 60										
Layer 61	39.1176667	37.0845	38.658	33.4936667	28.125	38.089	38.28672222	33.23588889	2.07084209	0.174195292
Layer 62										
Layer 63										
Layer 64	36.799	38.964	41.5346667	33.3103333	25.0085	36.17	39.09922222	31.49627778	2.35961337	0.142257884
Layer 65										
Layer 66										
Layer 67	38.7406667	39.481	37.966	34.1256667	30.2225	32.3693333	38.72922222	32.23916667	4.59332465	0.044272642
Layer 68										
Layer 69										
Layer 70										

***Supplementary Table 3**: Analysis of Pore Size Measurements made in X versus Z Direction for Porous Architecture C*

LAYER #	X1	X2	X3	Z1	Z2	Z3	Mean (X-direction)	Mean (Z-direction)	T-statistic	P-value
Layer 1	34.928	36.3876667	36.7396667	33.4953333	35.6496667	32.3983333	36.01844445	33.84777778	1.96671136	0.18810981
Layer 2										
Layer 3										
Layer 4										
Layer 5	37.6903333	36.6783333	34.848	35.448	35.2003333	37.0843333	36.40555555	35.91088889	0.35762186	0.75484028
Layer 6										
Layer 7										
Layer 8										
Layer 9	36.601	38.1846667	38.0216667	34.812	36.4413333	32.0736667	37.60244445	34.44233333	2.266926648	0.15156202
Layer 10										
Layer 11										
Layer 12										
Layer 13	36.887	35.195	37.5016667	35.6676667	38.532	32.961	36.52788889	35.72022222	0.353714975	0.75736005
Layer 14										
Layer 15										
Layer 16										
Layer 17	37.2723333	36.4416667	35.7106667	35.2533333	37.423	34.0373333	36.47488889	35.57122222	0.953468653	0.44098056
Layer 18										
Layer 19										
Layer 20										
Layer 21	34.8156667	35.5603333	37.114	37.06	37.1456667	34.4603333	35.83	36.222	-0.255429536	0.82225991
Layer 22										
Layer 23										
Layer 24										
Layer 25	37.59	38.358	34.8723333	36.7086667	37.5416667	33.8996667	36.94011111	36.05	19.63085405	0.00258485
Layer 26										
Layer 27										
Layer 28										
Layer 29	37.3103333	36.103	35.806	38.0956667	38.5993333	33.212	36.40644444	36.63566667	-0.153271701	0.89225151
Layer 30										
Layer 31										
Layer 32										
Layer 33	36.581	42.7396667	36.2153333	36.0776667	37.8856667	34.0173333	38.512	35.99355556	1.98912288	0.18499169
Layer 34										
Layer 35										
Layer 36										
Layer 37	37.0006667	40.0053333	33.057	34.4516667	40.086	31.1403333	36.68766667	35.226	1.844429798	0.20642495
Layer 38										
Layer 39										
Layer 40										
Layer 41	38.431	39.479	35.2806667	34.403	35.546	29.0693333	37.73022222	33.00611111	6.348616428	0.02392409
Layer 42										
Layer 43										
Layer 44										
Layer 45	36.9046667	38.58	38.487	38.8813333	35.152	34.1056667	37.99055556	36.04633333	0.982095835	0.42960298
Layer 46										
Layer 47										
Layer 48										
Layer 49	36.1476667	38.565	40.15	38.0973333	35.8326667	37.2943333	38.28755556	37.07477778	0.766793214	0.52335122
Layer 50										
Layer 51										
Layer 52										
Layer 53	38.9223333	41.0383333	37.4136667	37.787	39.982	31.2853333	39.12477778	36.35144444	1.653101091	0.24012363
Layer 54										
Layer 55										
Layer 56										
Layer 57	35.7763333	39.095	35.7336667	39.9986667	38.463	36.5463333	36.86833333	38.336	-1.019860188	0.41508111
Layer 58										
Layer 59										
Layer 60										
Layer 61	39.413	39.9956667	37.2903333	40.4893333	37.658	35.2373333	38.89966667	37.79488889	1.010177425	0.41875233
Layer 62										
Layer 63										
Layer 64										
Layer 65	40.1543333	41.339	36.3923333	39.0016667	38.901	34.8763333	39.29522222	37.593	4.449692897	0.04697539
Layer 66										
Layer 67										
Layer 68										
Layer 69										
Layer 70										

***Supplementary Table 4**: Analysis of Channel Region Size Measurements made in X versus Z Direction for Porous Architecture A*

Sample 1 Channel Region			Sample 2 Channel Region			Sample 3 Channel Region			Sample 1 Channel Region			Sample 2 Channel Region			Sample 3 Channel Region							
X-Direction	X-Direction	X-Direction	X-Direction	X-Direction	X-Direction	X-Direction	X-Direction	X-Direction	Z-Direction	Z-Direction	Z-Direction	Z-Direction	Z-Direction	Z-Direction	Z-Direction	Z-Direction	Z-Direction	Mean_X	Mean_Z	Shapiro_p_X	Shapiro_p_Z	P-Value
39.478	33.007	28.888	35.054	32.353	33.44	40.034	39.809	40.089	31.19	32.777	33.351	45.704	45.816	48.198	33.392	41.194	34.716	35.79467	38.482	0.11816	0.0644761	0.383261
36.149	33.374	33.559	32.353	34.44	39.414	33.184	37.714	41.44	34.484	30	38.888	42.0036	43.202	40.047	28.127	35.007	35.472	35.73633	36.35896	0.234347	0.7085764	0.759415
34.448	34.484	33.448	32.353	33.44	39.414	32.495	36.142	43.363	28.894	30.02	31.155	41.027	45.066	44.092	35.279	32.812	30.346	35.50967	35.41011	0.032661	0.0833783	1
43.333	28.894	31.744	32.353	41.142	39.514	37.11	37.877	36.413	30.02	29.528	33.888	39.802	46.937	42.741	37.376	35.691	31.676	36.48667	36.40656	0.885414	0.666983	0.970098
37.794	33.393	30.128	32.353	46.937	39.012	34.868	41.26	34.75	29.528	31.19	33.961	41.106	48.746	41.351	38.198	36.814	34.546	36.72167	37.27111	0.667056	0.7900856	0.75096
38.369	34.002	35.572	30.805	35.054	40.424	35.063	39.807	36.401	36.67	33.337	33.893	41.512	47.518	43.854	35.691	34.772	37.167	36.16633	38.26822	0.761361	0.1617821	0.313082
39.479	35.158	36.771	30.273	34.115	29.135	34.106	27.609	33.336	35.594	34.462	30.56	44.023	47.661	46.009	32.985	29.751	34.066	33.33133	37.23456	0.887439	0.1024942	0.206586
41.681	32.265	33.448	36.014	45.696	36.861	36.055	32.17	39.011	33.387	31.111	36.683	44.023	40.098	39.665	37.56	36.599	40.663	37.02233	37.75433	0.388716	0.9373409	0.674939
43.347	36.179	35.158	41.21	34.105	30.618	36.764	39.94	38.465	34.448	37.238	43.139	42.883	46.256	42.228	37.427	36.96	38.461	37.30956	39.89333	0.998016	0.5099845	0.292436
44.827	45.6	41.47	41.201	31.032	31.035	35.591	37.62	31.873	35.199	35.861	37.266	37.972	45.64	40.515	39.621	41.241	43.959	37.80544	39.69711	0.242584	0.7683536	0.550133
44.142	38.626	30.469	39.123	30.949	29.065	39.223	37.399	37.62	34.592	35.232	31.731	45.851	37.555	40.93	39.804	41.888	39.564	36.29067	38.57189	0.24356	0.9812102	0.304616
37.266	37.24	43.644	36.496	38.219	36.171	34.685	37.221	34.615	31.034	31.723	36.557	36.812	32.933	39.12	34.685	36.915	39.575	37.28411	35.48378	0.019431	0.5027786	0.207578
42.896	42.808	34.24	34.152	33.548	30.842	30.945	35.438	44.298	32.42	37.955	38.644	38.123	44.415	42.756	39.107	39.697	30.264	36.57411	38.15344	0.06005	0.4222433	0.62315
45.563	44.48	29.486	32.535	43.262	31.658	36.96	35.921	45.634	31.064	37.266	35.868	42.331	44.415	39.454	33.04	37.928	32.967	38.38878	37.14811	0.154404	0.834495	0.685254
42.068	38.675	33.453	35.745	34.757	28.519	33.008	45.055	32.985	37.24	35.178	35.232	44.844	48.698	37.344	34.106	30.789	36.28	36.02944	37.74567	0.633028	0.1132813	0.563066
44.827	38.841	29.942	36.441	36.137	32.58	36.878	34.083	28.619	44.874	41.378	35.967	42.323	39.836	43.161	33.588	39.564	39.046	35.372	39.97078	0.795796	0.8443005	0.015495
36.685	33.225	41.428	35.269	35.745	35.208	39.594	31.868	36.817	43.599	42.266	37.396	38.176	43.185	41.502	37.948	36.28	40.113	36.20433	40.05167	0.796805	0.4202229	0.028183
40.83	38.779	37.094	38.318	34.854	31.807	33.236	34.599	29.463	42.22	43.736	44.296	37.402	42.74	37.768	34.186	35.513	38.21	35.44222	39.56344	0.966223	0.3202226	0.008605
40.144	35.301	35.294	30.842	39.132	34.243	32.746	37.732	35.272	41.546	42.929	36.092	44.815	44.125	45.06	35.723	33.404	44.725	35.634	40.93544	0.821639	0.0368431	0.027344
37.396	33.333	36.046	41.615	31.977	31.273	35.209	34.229	35.272	35.986	38.069	41.522	40.39	44.958	38.664	42.04	37.347	36.967	35.15	39.54922	0.534837	0.6430397	0.019474
35.986	37.396	35.463	39.576	31.194	32.032	33.817	37.21	29.046	44.291	42.912	40.234	39.495	42.437	36.984	37.354	37.365	36.929	34.63556	39.77789	0.913249	0.1275784	0.003146
36.678	32.644	38.908	42.908	35.96	33.408	35.561	40.095	33.195	38.163	41.574	41.546	37.397	40.345	35.316	36.988	42.747	40.664	36.59522	39.41556	0.508199	0.5635349	0.073758
33.218	36.783	33.333	40.81	30.813	34.884	33.507	33.865	34.48	42.957	40.162	45.068	43.705	39.951	40.338	34.442	39.419	39.843	34.63256	40.65389	0.152283	0.3141516	0.000913
40.138	35.538	41.574	42.016	38.983	34.494	35.879	36.216	31.535	41.522	46.449	34.94	38.657	43.277	34.913	32.791	40.717	41.496	37.37478	39.418	0.661502	0.7122346	0.335528
40.138	35.538	41.574	43.715	37.545	30.278	35.803	37.841	27.878	41.522	46.449	34.94	43.697	39.531	35.294	29.507	31.189	32.822	36.70111	37.21678	0.73939	0.7212484	0.806934
44.296	40.138	42.305	37.919	31.319	34.531	34.33	31.453	46.595	42.912	33.477	37.094	39.246	38.786	34.623	45.137	39.94	31.516	38.09844	38.08122	0.525531	0.9509231	0.995168
41.528	42.912	40.138	32.511	35.894	31.061	34.976	36.929	32.368	35.294	33.91	39.452	38.336	42.116	35.872	36.536	40.666	33.735	36.47967	37.32411	0.526193	0.6044037	0.647807
42.22	41.528	38.754	34.23	33.375	32.353	30.429	34.857	33.236	44.988	38.908	35.993	38.342	36.669	37.537	39.869	39.004	30.472	35.66467	37.97578	0.217707	0.4257817	0.139248
38.754	41.546	40.83	38.712	31.375	35.179	33.651	34.025	31.709	38.761	36.704	36.704	41.614	36.137	41.239	37.768	37.427	36.988	36.19789	38.14911	0.33433	0.0482955	0.25
41.528	42.929	42.907	36.996	31.935	36.593	30.472	33.651	34.025	42.912	35.993	36.841	37.013	37.066	44.96	31.709	37.768	37.427	36.78178	37.96544	0.301377	0.1585663	0.498379
38.295	38.889	34.141	40.765	32.353	37.127	35.272	38.183	37.905	38.219	44.639	40.427	39.551	34.044	38.692	46.066	40.268	37.944	36.99222	39.98333	0.694527	0.5401827	0.048936
43.75	37.603	39.68	33.791	28.443	32.567	30.717	35.745	36.599	39.589	40.331	44.444	34.586	37.926	36.858	43.44	42.666	41.494	35.43278	40.14822	0.997076	0.9039881	0.019817
40.978	35.416	30.587	30.836	32.524	29.657	36.573	41.595	41.213	40.972	38.988	36.812	36.752	41.675	38.37	42.374	43.983	46.15	35.48656	40.67511	0.129978	0.7075664	0.000682
43.078	40.331	38.944	36.75	32.151	28.217	33.865	33.566	35.839	41.666	44.466	44.444	39.618	43.351	30	44.861	44.015	45.137	35.86011	41.95089	0.997278	0.0009182	0.007813
38.988	34.141	42.412	33.76	31.013	43.782	36.665	32.992	36.573	40.278	40.331	44.531	32.108	32.503	29.179	42.982	40.454	41.079	36.70289	38.16056	0.582199	0.1049275	0.532436

***Supplementary Table 5**: Analysis of Channel Region Size Measurements made in X versus Z Direction for Porous Architecture B*

Sample 1 Channel Region			Sample 2 Channel Region			Sample 3 Channel Region			Sample 1 Channel Region			Sample 2 Channel Region			Sample 3 Channel Region							
X-Direction	X-Direction	X-Direction	X-Direction	X-Direction	X-Direction	X-Direction	X-Direction	X-Direction	Z-Direction	Z-Direction	Z-Direction	Z-Direction	Z-Direction	Z-Direction	Z-Direction	Z-Direction	Z-Direction	Mean_X	Mean_Z	Shapiro_p_X	Shapiro_p_Z	P-Value
82.305	73.653	84.856	71.688	79.382	72.678	72.127	71.338	81.939	70.436	78.334	77.917	62.974	73.466	70.911	70.382	77.347	75.788	76.66289	73.06167	0.05743923	0.23422195	0.108016
80.633	81.743	69.308	72.847	75.788	75.145	72.083	77.918	73.805	77.945	85.001	77.5	78.704	72.46	66.209	74.685	72.383	75.689	75.47444	75.61956	0.895738006	0.870462537	0.939954
77.502	79.493	75.084	78.609	78.78	76.242	73.335	75.435	81.617	74.168	77.917	77.917	81.724	65.946	77.405	73.002	72.979	79.099	77.34411	75.573	0.980241954	0.394259423	0.297195
82.793	82.645	73.589	72.079	70.341	77.349	69.721	71.847	75.755	70.667	74.667	83.669	62.588	72.01	73.589	81.222	82.321	74.084	75.12433	74.97967	0.167451486	0.500471771	0.963169
77.077	88.149	66.872	74.494	82.985	77.444	68.884	72.463	75.722	77.667	70.34	83.677	62.431	77.753	78.208	73.488	81.402	81.222	76.01	76.24311	0.842072666	0.240104795	0.949168
79.687	80.904	75.368	74.879	67.439	76.794	77.13	73.382	76.161	76.345	72.667	78.368	61.97	98.22	79.021	74.593	77.931	74.587	75.74933	77.078	0.406987637	0.055773262	0.755217
74.78	82.882	64.179	80.403	73.918	75.574	70.667	73.333	71.71	74.528	75.834	75.417	63.362	77.9	71.182	77.292	82.948	73.941	74.16067	74.71156	0.822671115	0.39556542	0.858022
80.01	78.643	68.983	69.087	70.657	82.239	79.184	78.754	82.235	75.751	75.851	81.25	70.625	74.052	72.404	73.918	76.308	69.5	76.64356	74.40656	0.027905449	0.718579054	0.300781
74.658	80.654	72.749	84.85	71.104	74.447	76.676	71.744	75.555	67.91	75.004	72.917	66.056	72.361	68.927	72.763	79.545	68.891	75.82633	71.59711	0.226063296	0.665370166	0.118921
82.374	81.498	76.129	72.836	70.512	78.333	73.429	80.805	75.343	69.177	75.001	76.254	77.23	85.86	69.879	74.003	68.788	66.687	76.80656	73.65322	0.646101475	0.347106755	0.332488
80.108	71.773	70.144	73.612	75.673	70.02	80.004	77.926	70.362	72.935	70.834	80.433	66.719	75.778	75.462	65.919	71.591	66.687	74.40244	71.81756	0.124099389	0.538596153	0.319602
79.324	74.185	71.424	70.813	74.371	74.167	74.308	78.616	70.367	75.018	75.421	70.436	67.915	77.428	72.236	81.018	68.924	70.045	74.175	73.16011	0.180673122	0.616199851	0.530212
77.572	74.633	73.57	77.304	77.313	74.177	77.688	75.434	71.927	68.353	77.92	80.017	66.039	72.058	75.213	78.118	67.323	67.083	75.51311	72.45822	0.221596554	0.168603167	0.171849
71.744	80.936	73.22	64.921	72.053	72.936	73.92	78.32	69.269	74.486	70.413	75.72	70.287	77.316	72.481	72.593	68.111	75.094	73.03544	72.94456	0.777118027	0.896793902	0.966723
82.221	81.612	73.841	68.053	70.983	71.261	71.662	80.662	74.979	75.774	74.078	78.639	76.351	79.105	72.748	69.453	69.553	67.188	75.03044	73.65433	0.206607848	0.599547505	0.588935
81.427	75.846	74.817	75.347	66.504	68.899	72.502	75.595	71.112	69.558	72.021	72.84	67.992	84.619	78.864	73.352	72.99	68.095	73.561	73.37011	0.817325056	0.112445489	0.951173
73.807	81.188	71.794	69.87	74.496	71.814	75.326	72.446	73.205	70.8	79.016	72.457	66.448	80.205	75.652	73.468	77.827	79.27	73.77178	75.01589	0.106528215	0.489185005	0.378951
76.44	81.188	83.28	75.321	78.548	71.605	77.273	72.822	71.707	71.517	73.17	80.175	62.838	77.346	77.952	62.433	66.933	71.38	76.46489	71.52711	0.617524505	0.490091622	0.050321
79.611	73.004	77.591	68.459	73.097	75.435	72.325	76.877	72.147	69.421	74.38	80.165	62.428	85.861	79.798	66.576	69.633	80.004	74.28289	74.25178	0.854993403	0.66817373	0.990661
70.248	75.406	72.45	68.334	72.546	70.853	71.079	77.327	69.369	72.333	76.033	78.53	67.673	75.497	64.68	73.499	65.214	79.584	71.95689	72.56033	0.53010267	0.380997777	0.789074
68.675	80.408	74.838	65.829	73.137	73.761	73.967	78.621	72.626	77.704	78.117	80.182	66.368	73.027	73.776	72.408	69.061	73.761	73.54022	73.82267	0.746777236	0.794079959	0.872754
68.675	76.36	79.687	74.659	71.444	73.808	82.352	77.403	68.248	78.991	80.261	79.416	68.997	72.374	80.573	71.279	72.271	78.751	74.73733	75.87922	0.870217741	0.053986207	0.659266
69.544	77.002	70.834	71.261	72.812	81.668	70.589	70.293	70.459	80.251	77.741	80.742	60.692	71.653	69.431	67.188	82.093	77.957	72.718	74.19422	0.004977932	0.299143434	0.820313

***Supplementary Table 6**: Analysis of Channel Region Size Measurements made in X versus Z Direction for Porous Architecture C*

Sample 1 Channel Region			Sample 2 Channel Region			Sample 3 Channel Region			Sample 1 Channel Region			Sample 2 Channel Region			Sample 3 Channel Region							
X-Direction	X-Direction	X-Direction	X-Direction	X-Direction	X-Direction	X-Direction	X-Direction	X-Direction	Z-Direction	Z-Direction	Z-Direction	Z-Direction	Z-Direction	Z-Direction	Z-Direction	Z-Direction	Z-Direction	Mean_X	Mean_Z	Shapiro_p_X	Shapiro_p_Z	P-Value
115.571	111.099	109.909	118.978	118.034	112.88	111.922	116.717	120.174	110.245	98.379	112.704	103.962	111.865	113.976	123.271	117.564	107.043	115.031556	111.001	0.57677162	0.99723965	0.20633376
112.704	118.62	124.942	105.702	126.005	119.382	111.577	118.888	120.175	126.122	119.693	124.653	112.812	115.561	117.79	116.952	119.612	115.81	117.555	118.778333	0.57266909	0.5320307	0.60812346
120.923	132.858	118.691	112.915	119.744	108.748	100.35	108.305	124.424	113.389	108.015	105.997	115.641	119.45	112.778	112.302	116.587	116.828	116.328667	113.443	0.97390831	0.69833726	0.47213983
122.234	112.546	112.474	109.634	114.572	107.526	110.501	114.843	119.007	121.783	113.814	102.093	115.012	117.953	116.714	123.719	114.167	121.855	113.704111	116.345556	0.72316843	0.15960774	0.26821588
114.631	122.526	110.625	109.288	118.176	107.529	109.076	127.393	119.516	123.954	120.538	112.162	120.417	116.667	113.777	122.757	120.318	110.734	115.417778	117.924889	0.43825299	0.35637453	0.37649296
120.409	109.221	115.133	106.015	117.958	108.577	117.04	122.431	110.445	115.547	122.341	114.341	116.251	117.953	113.762	105.739	114.774	106.907	114.136556	114.179444	0.60946745	0.40033659	0.98773894
122.508	113.531	120.292	108.513	117.67	117.853	108.736	122.62	114.429	119.328	117.674	123.103	114.174	119.59	111.344	115.493	121.022	112.498	116.239111	117.136222	0.35422918	0.8404327	0.56153526
114.263	117.871	110.13	110.285	121.487	119.734	108.832	119.641	119.287	113.392	123.852	113.918	110.02	115.465	113.334	127.672	122.052	116.281	115.725556	117.331778	0.10630365	0.30260557	0.54905545
111.185	116.005	114.682	109.622	109.014	124.2	104.71	112.798	123.207	111.715	121.35	126.011	104.187	120.018	110.003	117.777	118.654	118.77	113.935889	116.498333	0.56179708	0.59483302	0.42694767
122.03	117.11	120.044	108.238	113.996	104.894	118.868	113.317	121.797	114.227	115.484	123.884	105.457	114.586	108.751	113.893	118.322	114.665	115.588222	114.363222	0.36789447	0.53810155	0.47058532
119.704	127.87	111.815	112.643	113.931	107.409	115.395	110.162	117.737	119.832	121.52	108.864	114.286	114.755	109.257	114.537	113.856	121.422	115.185111	115.369889	0.5572896	0.21071467	0.86802235
115.71	114.002	116.752	110.485	118.618	119.718	113.423	115.376	115.785	108.864	112.678	113.505	115.188	110.569	111.86	110.013	112.558	125.374	115.541	113.401	0.92842233	0.00788849	0.359375
113.201	122.093	113.768	114.033	114.165	111.345	113.663	114.171	107.75	113.515	114.771	116.881	117.264	113.032	109.283	112.322	111.893	121.888	113.798778	114.538778	0.03414727	0.72244948	1
122.093	113.768	122.779	111.502	115.3	118.891	112.746	110.577	110.587	120.368	119.832	121.52	107.575	118.078	102.94	105.573	108.598	107.212	115.360333	112.410667	0.12797503	0.07595816	0.19124659
114.045	121.091	124.713	108.668	108.044	110.28	112.511	120.925	111.115	112.618	113.445	116.399	107.995	111.771	108.826	111.62	110.566	112.291	114.599111	111.725667	0.17151135	0.84169346	0.10772054
114.596	112.433	126.18	114.665	117.732	123.229	115.483	121.394	120.355	115.154	113.465	119.34	116.843	114.717	112.632	114.825	115.709	116.589	118.451889	115.474889	0.68312877	0.85193217	0.06642717
117.765	116.308	114.545	118.863	123.298	118.218	121.845	111.909	119.29	119.388	124.132	123.564	108.35	113.406	109.164	111.744	109.728	110.324	118.004556	114.422222	0.96806294	0.04732411	0.12890625

Supplementary Figure 1: *Channel region size differences in both X and Z directions for all porous architectures.*

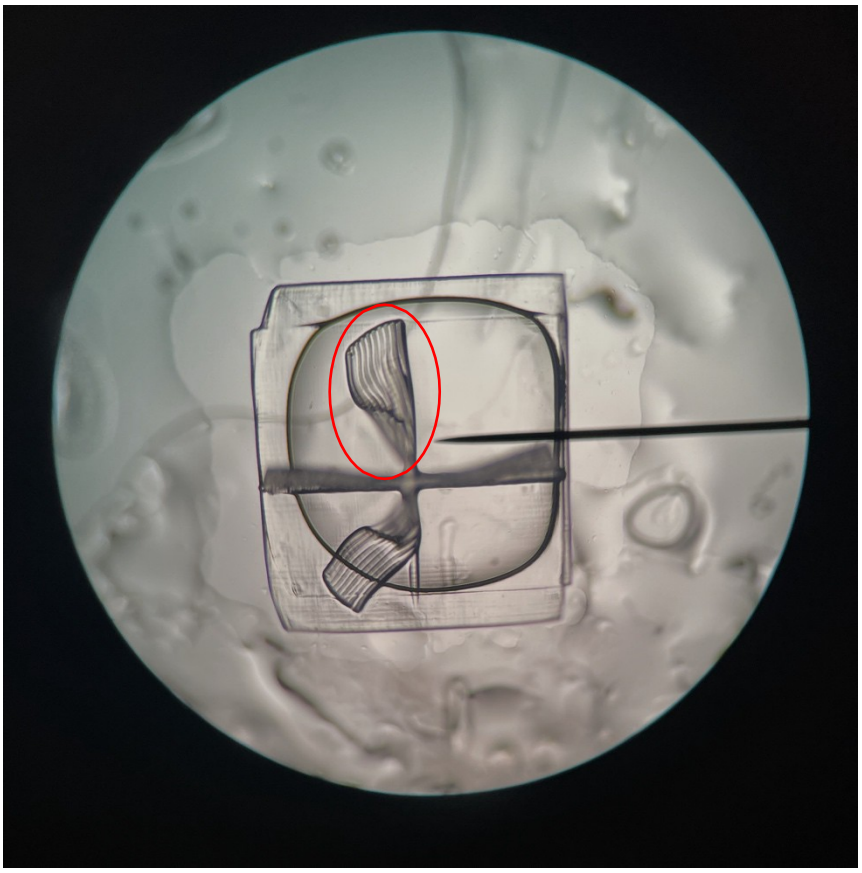

Supplementary Figure 2: *Image of the sacrificial support structure attempted after the printing issues were identified. The support structure is unfortunately warped, and highlighted in the circled region, it's possible to see that each layer is not being deposited directly on top of the preceding layer, but rather is being formed slightly off center, which led to this "tilting" behavior.*

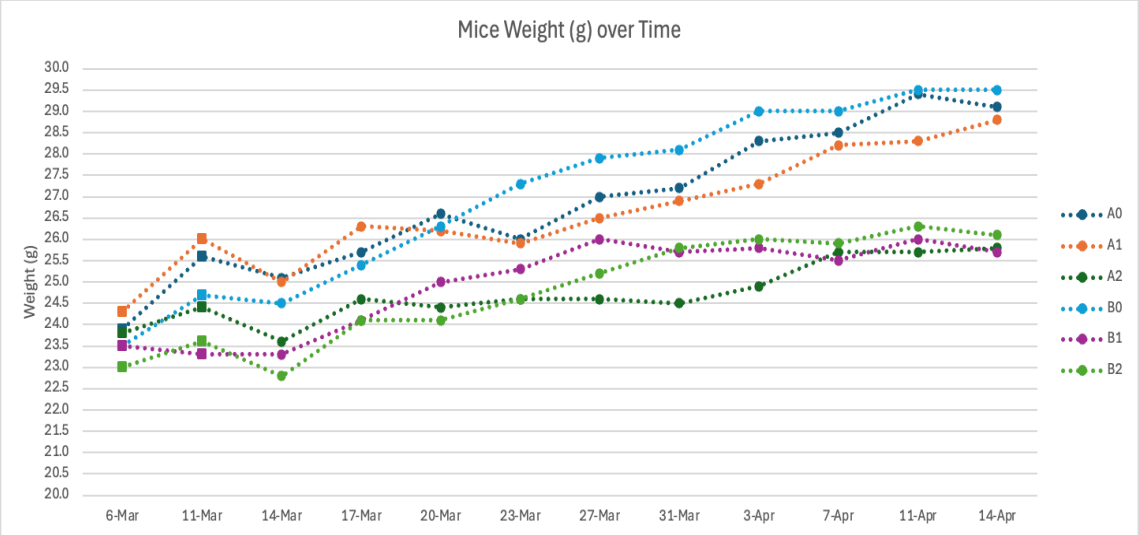

Supplementary Figure 3*: Recorded weights of all mice used in the study, over the four-week period. Mice were weighted twice a week. The day of the implant was March 12th, and the day the mice samples were harvested was April 14th.*

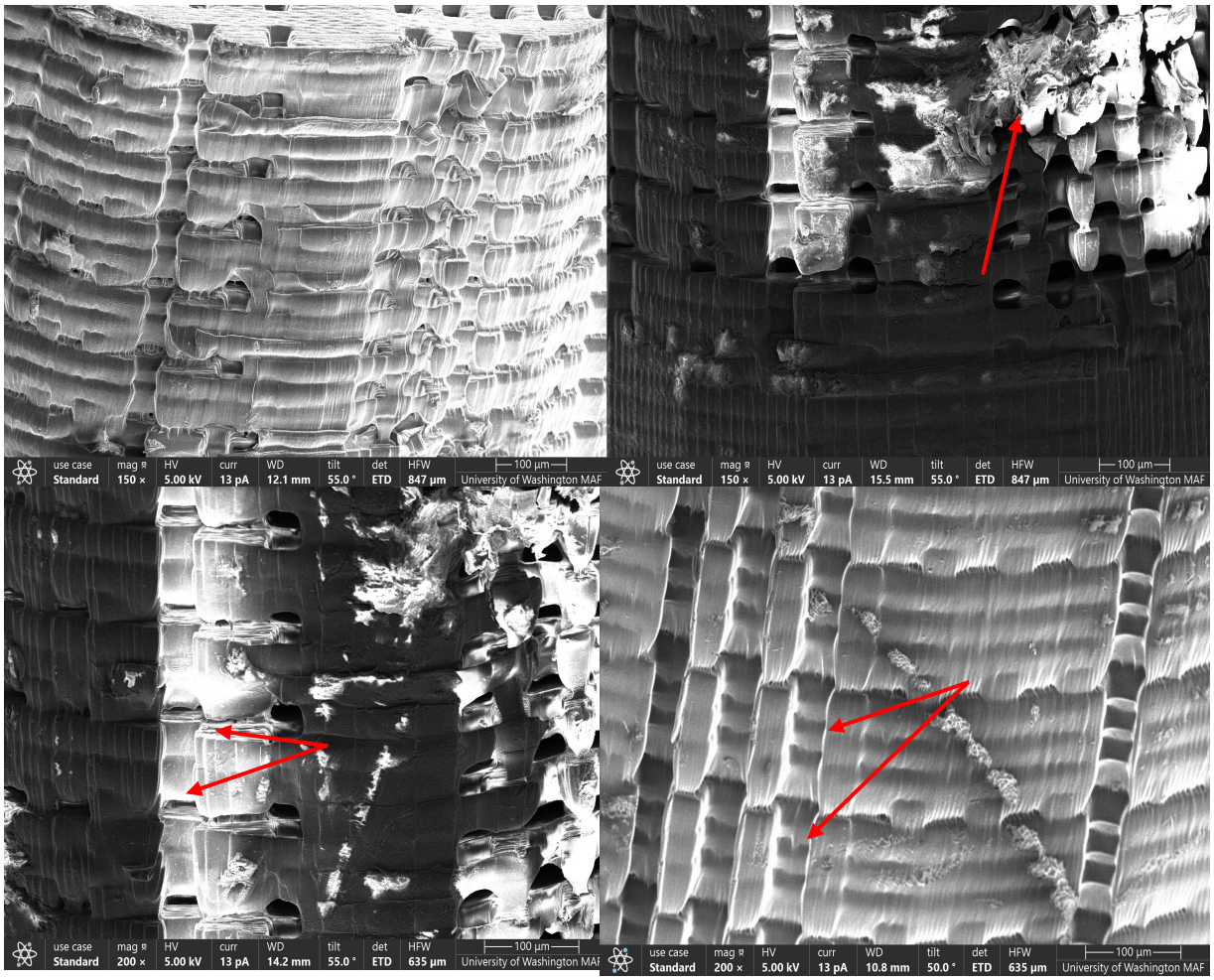

Supplementary Figure 4: *Boundary artifacts shown with red arrows that may have impacted the ability of the cells to infiltrate into the scaffold*